Mean streaming and the onset of turbulence in the reciprocating flow in a double bifurcation airway model: Insights for high-frequency ventilation

Chinthaka Jacob ⬤,[1,*] David G. Tingay,[2] and Justin S. Leontini[1]

[1]*Faculty of Science, Engineering and Technology, Swinburne University of Technology, Melbourne, Victoria 3122, Australia*
[2]*Neonatology, The Royal Children's Hospital, Melbourne, Victoria 3052, Australia*

This paper reports on a numerical study of the reciprocating flow through a double bifurcation. Its aim is to quantify the potential gas transport in flows similar to those in the human airway during high-frequency ventilation, a medical ventilation technique that uses fast, yet shallow, inflations to minimize pressure and volume variation in the lungs and therefore protect lungs from ventilator-induced lung injury. The shallow inflations mean that gas transport is not achieved by bulk advection and other mechanisms must be used. Here we focus on nonlinear mean streaming and turbulent diffusion. We show that both of these mechanisms are driven by the formation of Dean vortices due to centrifugal instability in the curved sections of the bifurcation. We report the impact of the upstream and downstream conditions on both of these during both inhalation and exhalation portions of the reciprocating flow; in particular, we show that the development of turbulence in a given airway vessel is influenced by downstream conditions and not simply by the local flow conditions. This result highlights the importance of using a geometry of appropriate complexity for the modeling of physiological flows, particularly if the results are to be parameterised for use in larger-scale but lower-order models.

I. INTRODUCTION

This paper reports on direct numerical simulations of the reciprocating flow through an in-plane double bifurcating tube. The primary objective of this paper is to provide a generic model of the flows and subsequent gas transport in the human airway at conditions that are typically experienced during high-frequency ventilation (HFV) [1], a type of mechanical ventilation therapy commonly used in the neonatal intensive care unit. HFV uses fast, low-tidal-volume inflations to achieve adequate gas exchange while simultaneously reducing peak intralung pressures to minimize overdistension and ventilator-induced injury. The low-tidal-volume inflations do not empty and refill the "dead space" of the airway and the success of HFV—or lack thereof—is therefore dependent on exploiting transport mechanisms other than bulk advection. Despite its extensive use and importance, the process of deliberately manipulating and optimizing the subtle gas exchange mechanisms involved in HFV are not completely understood [2].

Six such mechanisms are typically reported as operating during HFV [1,3]. Here we focus on two of these mechanisms due to their likelihood to provide gas transport over a range of scales: nonlinear mean streaming, the mean recirculation of fluid caused by a nonzero mean flow (noting that this occurs while the mean flux is zero in a purely reciprocating flow), and turbulent diffusion.

---

*Corresponding author: chinthaka.ravinatha@gmail.com

Further, we make a distinction between nonlinear mean streaming and mean drift or Lagrangian transport, which can be conflated in the literature.

Quantifying and understanding these transport mechanisms requires measurement of the flow field in geometries (and for flow parameters) that generate the flow structures that are responsible for the transport. A number of recent studies, therefore, take the approach of deriving geometry from medical imaging of selected regions of the airway, typically the large upper vessels which can be most accurately imaged. Choi *et al.* [4] presented a study of convective mixing during HFV in geometries derived from computed tomography (CT) of the first seven airway generations using large-eddy simulation. Roth *et al.* [5] presented a highly resolved computational study of HFV using geometry derived from magnetic resonance imaging of the first four airway generations, and flow rates from infant lung function testing, which clearly shows all of the six reported transport mechanisms for HFV operating in different regions of the airway. Jalal *et al.* [6] presented an experimental study based on magnetic resonance velocimetry of both steady and oscillatory flows (including at conditions relevant to HFV) in geometry derived from CT of the first three airway generations of real patients, and one aspect of the subsequent analysis quantifies the transport due to streaming.

Examples of imaging-derived geometry being used for airway modeling of non-HFV flows in the upper airway include the computational study of Luo and Liu [7], the experimental studies investigating steady and oscillatory flows in the upper airway of Banko *et al.* [8,9], and experimental studies investigating airway injury during medical ventilation [10].

Drawbacks of physiologically realistic geometries are the complexity, which leads to large computational models, and the fact that they are patient specific, which can make understanding the general flow physics difficult. Therefore, a second approach is to use idealized geometries which can be systematically studied and compared. The Weibel model [11] consisting of a series of generations where each generation is marked by the division of each airway vessel into smaller vessels is extensively employed. Recent computational studies of airway flows using this model include the flow-path-ensemble methods of Nowak *et al.* [12], Walters and Luke [13], Kleinstreuer and Zhang [14], which chain together a number of subunits consisting of only a small number of generations each to build up a single large flow path. Notably, Jalal *et al.* [15,16] use this geometry to conduct experimental flow studies at parameters relevant to HFV of an isolated double bifurcation—a comparison with the work of the same authors in physiologically realistic geometries shows many of the same qualitative flow features (noting that there is a quantitative difference in the measured transport).

A number of earlier studies using various other idealized bifurcation models have been conducted which are relevant to HFV; see the study Menon *et al.* [17] for high-frequency reciprocating flows in a 1:3 bifurcation model investigating flow distribution between lobar bronchi, supported by the early numerical study of Gatlin *et al.* [18] and the extensive combined numerical and experimental study of Bauer *et al.* [2] comparing conventional and HFV.

All these studies of both physiologically realistic and idealized geometries highlight the importance of the formation of Dean vortices via centrifugal instability [19], which form downstream of curved sections of the geometry and impact both the mean streaming and formation of turbulence.

With respect to mean streaming, these streamwise-oriented vortices can generate a strong secondary flow (i.e., a flow in the nonstreamwise directions), which is a function of the upstream conditions. This Dean-vortex-generated secondary flow is the fundamental cause of nonlinear mean streaming during a reciprocating flow; the secondary flow generated at a given location during inhalation is not equal and opposite to that generated during exhalation, and the difference leads to a nonzero mean. Our own previous work in a single bifurcation [20] clearly showed the difference in Dean vortex structure leaving a bifurcation between an inhalation and exhalation flow. There does not appear to be existing quantitative data on the amount of transport that can be generated by mean streaming in bifurcating geometries as a function of the geometric and flow parameters.

With respect to turbulence, the presence of these vortices also fundamentally changes the stability characteristics and the onset of turbulence in the flow when compared with the flow in a straight

pipe. At high frequencies, reciprocating flows in straight pipes have recently been shown to become unstable via bypass transition (which is a nonlinear phenomenon) [21], driven by the growth of disturbances at the pipe wall in the Stokes layer [22–24], with turbulent bursts occurring at phases of maximum *deceleration* (i.e., when the instantaneous *flow rate* is near zero for a sinusoidal oscillation). Recent numerical studies in toroidal [25], helical [26], and bent [27] pipes have shown linear processes can lead to instability due to the growth of perturbations of the streamwise vortices caused by the curvature. Our own work studying the reciprocating flow in a single bifurcation [20] shows a similar outcome; turbulent bursts occur in regions downstream of the bifurcation after the appearance of Dean vortices and at times when the instantaneous *flow rate* is maximized (i.e., when the bulk *acceleration* is near zero for a sinusoidal oscillation).

We note here that the difference between the inhalation and exhalation flow structure indicates that the minimal geometry that can be used to quantify gas transport in a given airway vessel consists of at least two generations. There needs to be a bifurcation both upstream and downstream during both inhalation and exhalation. While single bifurcation studies can be used to elucidate fundamental processes (see, for example, our previous work [20], and others including Pedley [28], Jan *et al.* [29], and Heraty *et al.* [30]), they cannot capture the coupling between inhalation and exhalation flows that is inherent in high-frequency reciprocating flows.

Therefore, this paper reports on direct numerical simulations of reciprocating flows in a double bifurcation. The geometry used is self-similar, with a proportional reduction in the vessel diameter and length at each generation, and follows the proportions outlined from physiological data by Grotberg [31]. This assumption of self-similarity also means different generations of the overall airway can be simulated by simply changing the bulk flow parameters (if it is assumed the coupling between generations that are not direct neighbors is negligible). Further, the local bulk flow parameters can be calculated at each generation once the parameters at the primary generation are fixed. We have conducted simulations corresponding to the bulk flow conditions in the first nine generations of the airway, taking our primary conditions as those used to ventilate a typical full-term neonate at the extremes of the parameters typically used during HFV.

First, we show that mean streaming is significant for conditions modeling the first five generations of the airway. We note that the experimental study in a similar double bifurcation model of Jalal *et al.* [6] reported that the recirculating flow rate due to mean streaming is much less than the peak bulk flow rate, leading the authors to conclude that mean streaming is not a significant contributor to ventilation. Our results agree, however, our interpretation does not, as we show that even this weak streaming can be enough to provide adequate oxygen to a patient, at least across these first five generations. We note that this result is in qualitative agreement with our previous single-bifurcation results [20] but is quantitatively more informative, as it captures the coupling effect between generations.

Second, we show that, as indicated in our previous single-bifurcation study [20], conditional turbulence arises in cases modeling the first three airway generations, at instants where the flow rate is near its maximum and apparently via an instability of the streamwise Dean vortices. However, the modification of the flow upstream *and* downstream due to the presence of other generations has a strong impact on the onset and sustained production of turbulence.

A. Methodology

1. Flow domain and geometry configuration

The geometry employed throughout this paper is a 1:2:4 symmetric planar bifurcating pipe. The human airway consists of 21 successively bifurcating generations [32,33], and the geometry of these bifurcations is approximately geometrically similar, maintaining a constant ratio between the diameters of a predecessor pipe D_i and a successor pipe D_{i+1} of $D_{i+1}/D_i = 0.79$, and an included angle between the bifurcated successor pipes around $\Theta = 64°$ [31]. Figure 1 shows a schematic of the geometry employed. Pertinent to this geometry module, the branches from the top to bottom of the hierarchy are referred to as the mother branch, daughter branches, and granddaughter branches.
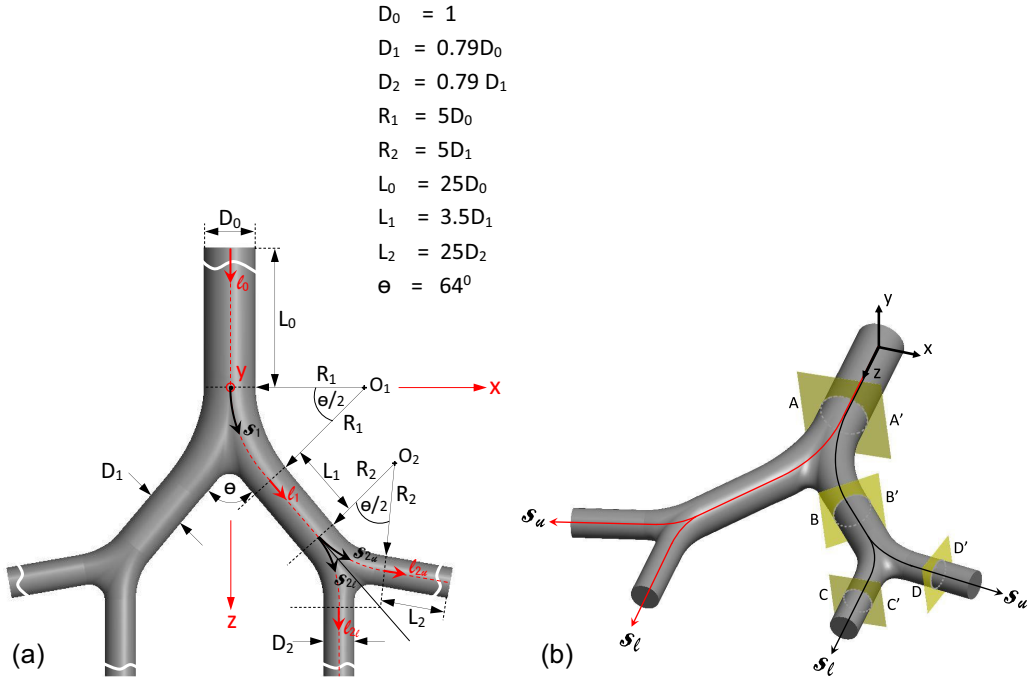
FIG. 1. Attributes of the bifurcation model used in the paper. (a) Dimensions of the planar 1:2:4 bifurcation. (b) Three-dimensional CAD model of the 1:2:4 bifurcation. Note that the CAD model shown here is not to scale and the actual computational domain has much longer inlet and outlet sections to minimize the effect of boundary conditions on the flow generated by the bifurcation. D_0 corresponds to the diameter of the endotracheal tube of 3 mm.

Another aspect of the geometric similarity of the airway is the length of each branch section at the generation level i being approximately $3.5D_i$, where D_i is the diameter of the corresponding branch section. While we have used this length for the intermediate (daughter) branches, we have used very long inlet and outlet sections in our computational geometry to focus on the flow features generated by bifurcating junctions and the intermediate generation without the influence of the boundary conditions.

The centerline of the mother branch coincides with the z axis of the global coordinate system and splits into the two centerlines of the daughter branches. Each of these two centerlines of the daughter branches further splits into two, creating a total of four centerlines of the granddaughter branches. These centerlines coincide with branch axes in the cylindrical parts of the domain. Each axis of the successor branch is connected to its predecessor branch by a smooth linearly varying arc (such that the radius of curvature of the outermost surface of the geometry is constant) to obtain the centerlines of the bifurcating region. These centerlines, denoted by S, with subscripts u and l indicating upper and lower branches, are used to identify streamwise locations of various cross sections. In this context, the axial velocity of any arbitrary point in the fluid domain is defined as the tangential component of the velocity vector to the closest centerline point. Therefore, the axial velocity $\mathbf{U}_{\mathrm{ax}}$ is identical to the streamwise velocity of the point of interest. The transverse velocity $\mathbf{U}_{\mathrm{tr}}$ is the projection of the velocity vector in a plane perpendicular to $\mathbf{U}_{\mathrm{ax}}$.

2. Boundary conditions

Standard no-slip boundary conditions were applied at the rigid walls of the bifurcation, i.e., $\mathbf{u} = 0$ and $\partial p/\partial \mathbf{n} = 0$, where $\mathbf{u}$ is the flow velocity, p is the pressure, and $\mathbf{n}$ is the normal vector. Note

that the use of rigid walls is somewhat justified physiologically, as the upper airway is cartilage-reinforced and reasonably stiff [34].

The reciprocating flow with zero mean flux was driven by imposing a time-dependent boundary condition at the inlet (the free end of the mother branch) for the velocity, which was the analytical solution for the fully developed laminar reciprocating flow in an infinitely long straight pipe first derived by Womersley [35]. A zero-normal-gradient condition ($\partial p/\partial \mathbf{n} = 0$) was imposed for the pressure. We note that the use of $\partial p/\partial \mathbf{n} = 0$ means this is not a one-dimensional solution of the Navier-Stokes equations, however, *a postiori* checks show that this has a very small impact on the flow, which relaxes to the Womersley solution within a few diameters of the boundary.

We use the term inhalation to refer to the flow moving from upper generations to lower generations (i.e., from the mother branch to daughter and granddaughter branches), and exhalation to refer to the flow moving in the opposite direction.

At the free end of the granddaughter branches, a modified outflow condition was imposed. Here a Dirichlet condition was imposed on the pressure ($p = 0$), while nominally a zero-normal-gradient condition was imposed on the velocity ($\partial \mathbf{u}/\partial \mathbf{n} = 0$). However, an extra divergence term was added to the velocity to prevent flow entering the domain through this boundary which numerically stabilizes the solution. Locally, this means the mass conservation was not satisfied; however, the impact of this was evident only within $3 - 4$ diameters of the boundary, and the use of long granddaughter sections means this did not pollute the simulation results near the bifurcation.

We have previously used these boundary conditions successfully in studies of the reciprocating flow in a 1:2 bifurcation [20]. Further, the modified outflow boundary condition has previously been used successfully in other biologically inspired oscillating flows in the same code [36].

3. Discretization and solver details

The three-dimensional incompressible Navier-Stokes equations were solved in the flow domain described in Sec. I A 1 with the boundary conditions described in Sec. I A 2 using the spectral-element code NEK5000 [37]. The code has previously been employed and validated for use in oscillatory confined flows [38,39], including our own study of the reciprocating flow in a single bifurcation [20]. Further implementation details can be found in Tufo and Fischer [40], while an overview of the essential elements of the numerical scheme is provided below.

The code solves the incompressible Navier-Stokes equations in variational form, employing high-order tensor-product Lagrange polynomials over each element as both trial and test functions. Here, the order of the polynomials was used to control the resolution; for simulations of turbulent flows, we employed 12th-order polynomials, whereas for laminar flows we employed eighth-order polynomials for computational efficiency. These trial functions were associated with Gauss-Legendre-Lobatto quadrature points in each hexahedral element, noting that these elements could have curved faces to conform to the surface of the bifurcation geometry. A resolution study was conducted (see Appendix for more details), settling on a macroelement mesh of 49 920 elements. With the employed 12th-order polynomials, this results in 66 443 520 node points. This system was typically solved using 32 nodes, each containing two 16-core Intel Skylake CPUs for a total of 1024 cores with wall times of around one week to resolve a full reciprocation cycle. The first cycle was discarded to avoid the impact of any flow transient.

4. Simulation parameters

Since the geometry used is fixed, and the reciprocating flow employed is purely harmonic, the flow can be shown to be a function of only two nondimensional groups. The first of these essentially quantifies the amplitude of the reciprocating flow, which we define as a maximum Reynolds number,

$$\mathrm{Re}_{\max} = \widehat{U}_{\max} D_0/\nu, \tag{1}$$

TABLE I. Summary of simulation parameters used for the nine cases simulated.

Case $^{i-1}G_{i+1}$	Re_{max}	α^2
$^{0}G_2$	9600	11.31
$^{1}G_3$	6076	7.06
$^{2}G_4$	3846	4.41
$^{3}G_5$	2434	2.75
$^{4}G_6$	1512	1.72
$^{5}G_7$	953	1.07
$^{6}G_8$	600	0.67
$^{7}G_9$	378	0.42
$^{8}G_{10}$	247	0.26

where ν is the kinematic viscosity. The second parameter quantifies the frequency, which can be presented in terms of the square of the Womersley number,

$$\alpha^2 = \frac{2\pi f D_0^2}{4\nu},\tag{2}$$

where f is the frequency of oscillation.

To set these parameters to be clinically relevant, we start from a set of conditions of a typical full-term neonate, which are volume per inflation per unit body weight of the infant $1 - 3$ ml/kg and the frequency of therapy in the range of $5 - 15$ Hz [41]. The typical diameter of the endotracheal tube employed is 3 mm. Assuming typical numbers of a body mass of 3kg and a ventilator frequency of 12 Hz results in $Re_{max} = 9600$ and $\alpha^2 = 11.31$ at the mother branch of the first generation, referred to here as $^{0}G_2$.

The maximum local Reynolds number decreases from the predecessor generation Re_i to the successive generation Re_{i+1} by a factor of $D_i/(2D_{i+1}) \approx 0.63$ while the Womersley number decreases from the predecessor generation α_i to the successive generation α_{i+1} by a factor of $D_{i+1}/D_i = 0.79$. This reduction of Re_i and α_i with increasing generation number i is caused by the reduction of the local diameter in a given airway branch but an increase in the total area of each successive generation leading to a reduction of the local maximum velocity.

We therefore characterize the airflow at a particular airway generation subjected to HFV as a two-parameter problem in the $Re_{max} - \alpha^2$ space. If coupling between generations more distant than immediate neighbors is ignored, then the flow at a given generation is fully defined by these two parameters. Table I outlines the Re_{max}, α^2 pairs used for the cases of this paper. We have used pairs to run simulations matching the conditions of the first nine generations.

B. Results and discussion

1. Mean flow characteristics

The streaming velocity field is simply the cycle average of the velocity field, $\overline{\mathbf{u}}$, which is directly calculated by averaging over the second cycle of the flow simulation. We excluded the first cycle of the simulation to avoid any initial transient. We also note that any transient did not appear to extend beyond this first cycle, with the statistics of the flow apparently settled from the second cycle onward. In this context, the timescale of the oscillation of the flow cycle is much longer than the advective timescale L_{dom}/U where L_{dom} is the length of the computational domain. Therefore, we conclude that any transient appears in the flow has many advective time units to wash out of the domain even in a single cycle of oscillation.

The streaming velocity field for cases $^{0}G_2$, $^{1}G_3$, $^{2}G_4$, and $^{8}G_{10}$ are shown in Fig. 2. This figure presents contours of the streaming velocity component aligned with the local axial direction (the tangential component of the velocity vector to the closest centerline point) $\overline{\mathbf{U}}_{ax}$ with positive $\overline{\mathbf{U}}_{ax}$
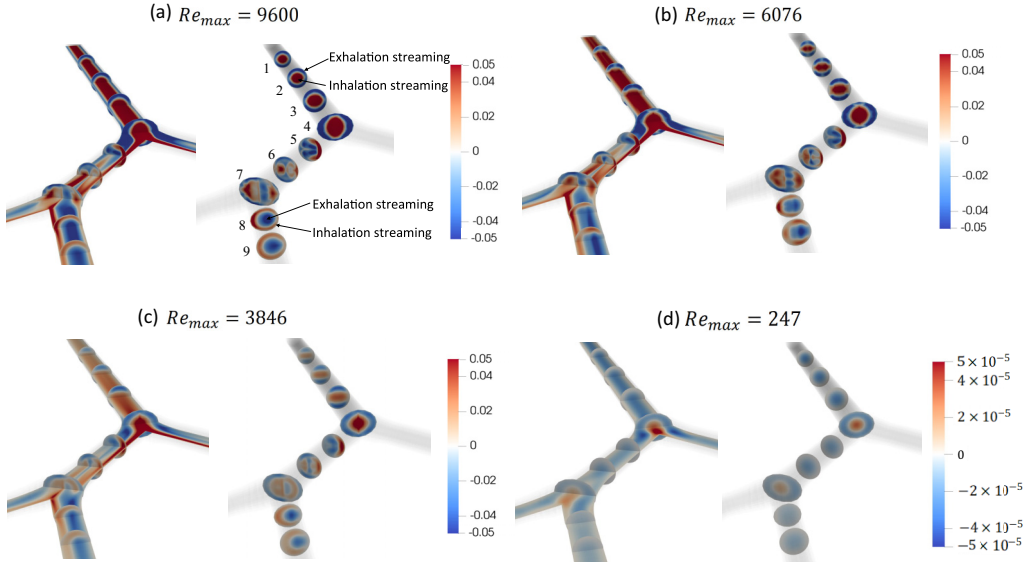
FIG. 2. Visualization of dimensionless mean streaming velocity $\overline{\mathbf{U}}_{ax}/\widehat{U}_{max}$ fields for (a) $^0G_2$, (Re_{max} = 9600, α = 3.36, L/a = 849); (b) $^1G_3$, (Re_{max} = 6076, α = 2.66, L/a = 861); (c) $^2G_4$, (Re_{max} = 3846, α = 2.1, L/a = 873); and (d) $^8G_{10}$, (Re_{max} = 247, α = 0.51, L/a = 950). The first panel of each case shows the longitudinal symmetry plane along with several transverse planes. The second panel shows the same field without the longitudinal symmetry plane.

designating inhalation. In each of the four cases, the first panel displays nine sections perpendicular to the streamwise direction accompanied by a plane passing through centerlines of all the branches. The second panel shows the same data without the latter center plane to clearly show the structure on the perpendicular planes. Note that the integral of $\overline{\mathbf{U}}_{ax}$ over an arbitrary cross section is zero as the $\overline{\mathbf{U}}_{ax}$ field is computed from the cycle average of the zero-net-mass-flux reciprocating flow.

Figures 3(a)–3(c) show the mean flow axial vorticity $\overline{\omega}_{ax}$. Its structure is qualitatively similar between the $^0G_2$, $^1G_3$, and $^2G_4$ cases. A general characteristic of these three cases is that along the core of the mother branch there are eight counter-rotating vortices near the bifurcating junction, decaying to four counter-rotating vortices away from the bifurcation. These eight counter-rotating vortices appear as a consequence of merging four counter-rotating vortices from each of the two daughter branches in the exhalation flow. Along the core of the daughter branches, there are four counter-rotating vortices. Along the core of the granddaughter branches, there are four counter-rotating vortices near the bifurcating junction and their strength decreases with the distance measured from the bifurcating junction.

The vortex structure composed of four counter-rotating vortices observed in the mother branch (at least at a short distance away from the bifurcation of Figs. 3(a)–3(c) is qualitatively similar to thhe structure we have previously reported for the single bifurcation [20]. Further, the vortex structure composed of two counter-rotating vortices observed in the granddaughter branches of Figs. 3(a)–3(c) is qualitatively similar to the vortex structure in the daughter branches of a single bifurcation [20]. The fact that the addition of an extra generation has only a minor impact on the mean flow structure suggests that intergenerational coupling is likely to be weak beyond one generation and the double bifurcation likely captures the essential qualities of the flow in the airway. Therefore, the streaming flow in the intermediate vessel provides a good measure of the capacity for gas transport between generations via mean streaming.

The structure of the streaming flow in the intermediate branches of the first three cases [Figs. 2(a)–2(c)] is such that along the inner core there is a vertical semiannular region of inhalation
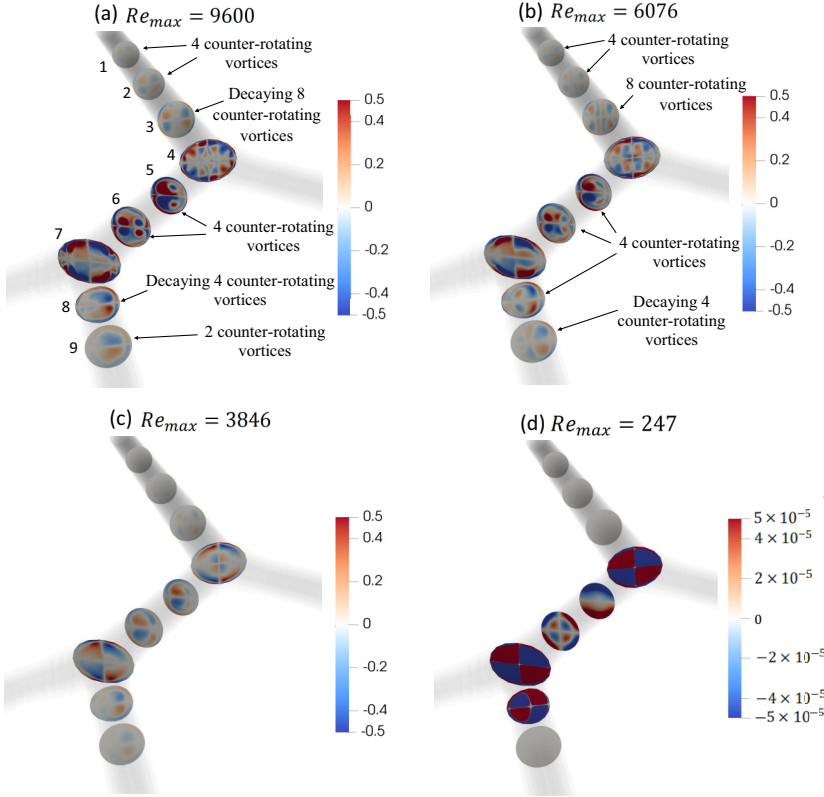
FIG. 3. Visualization of dimensionless axial vorticity $\overline{\omega}_{ax}/\overline{\omega}_{max}$ (where $\overline{\omega}_{max} = \hat{U}_{max}/D_0$), computed based on the mean streaming velocity $\overline{\mathbf{U}}_{ax}$ fields for (a) $^0G_2$, (Re$_{max}$ = 9600, α = 3.36, L/a = 849); (b) $^1G_3$, (Re$_{max}$ = 6076, α = 2.66, L/a = 861); (c) $^2G_4$, (Re$_{max}$ = 3846, α = 2.1, L/a = 873); and (d) $^8G_{10}$, (Re$_{max}$ = 247, α = 0.51, L/a = 950).

streaming located along the wall at the outside of the turn, which is weakening in the direction of section 5 to 6. Simultaneously, there is another circular region of inhalation streaming closer to the wall at the inside of the turn, which is strengthening in the same direction. Concurrently, there is a region of exhalation streaming that surrounds these two regions of inhalation streaming. This exhalation streaming region eventually diffuses along the horizontal centreline from section 5 to 6. This streaming flow distribution can be ascribed to the evolving vortices shown by sections 5 and 6 of Figs. 3(a)–3(c). There are two strong counter-rotating vortices accompanied by another two relatively weak counter-rotating vortices in section 5 and they adjust to approximately equal strengths in section 6. The appearance of these vortices can be further ascribed to the formation of two counter-rotating vortices in the inhalation flow and four counter-rotating vortices in the exhalation flow pertaining to the evolution of the instantaneous axial vorticity as shown in Sec. I B 4.

While there is evidently a strong streaming flow in the upper generations, this is not the case in the lower generations. Figure 3(d) shows case $^8G_{10}$, and it is clear that in this case the streaming is negligible (note that the color map range is 10^3 times smaller here).

These observations reveal the formation of longitudinal vortices. To further investigate this, Fig. 4 shows the secondary velocity vector field $\mathbf{U}_{tr}$ superposed on contours of the streaming velocity $\overline{\mathbf{U}}_{ax}$ on corresponding sample planes in the mother, daughter, and granddaughter branches. The figure clearly shows that the lobes of high $\overline{\mathbf{U}}_{ax}$ coincide with recirculation regions in the secondary flow.
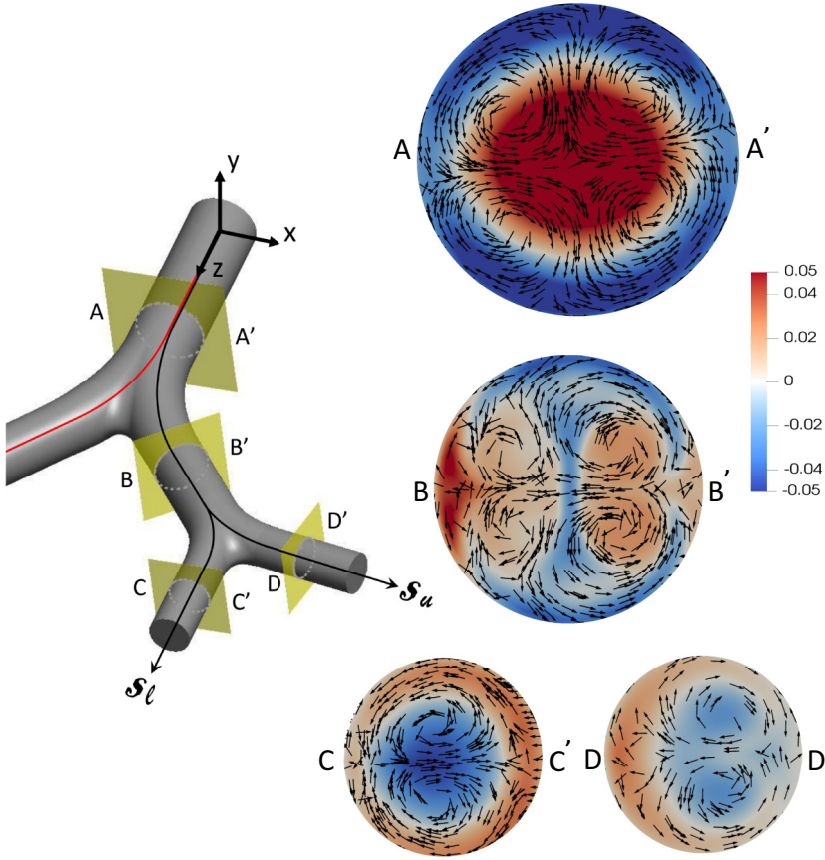
FIG. 4. Contours of dimensionless streaming velocity $\overline{\mathbf{U}}_{\mathrm{ax}}/\widehat{U}_{\mathrm{max}}$ fields on cross sections A-A′, B-B′, C-C′, and D-D′ superposed with secondary flow vectors $\mathbf{U}_{\mathrm{tr}}$. Note the vectors are uniform length, not scaled by magnitude, and so indicate the flow direction only. Cross sections A-A′, B-B′, C-C′, and D-D′ are located at the middle of the straight section at each generation level.

2. Recirculation and mean streaming

Here, the amount of flow recirculated is quantified by using the positive flux of the cycle-averaged axial (streaming) velocity field $\overline{\mathbf{U}}_{\mathrm{ax}}$. Essentially, over an arbitrary plane of interest, the flux over the portions where the flow is moving in one normal direction is equal and opposite to the flux over the portions where the flow is in the opposite normal direction. This is due to the fact that the overall mean flux must be zero across an arbitrary plane of interest in a zero-net-mass-flux reciprocating flow. The amount of recirculating flux across a given plane of interest is computed by integrating the positive portions of velocity across the area normal to that positive velocity profile, given by

$$Q_r = \int_A \overline{\mathbf{U}}_{\mathrm{ax}} \cdot \widehat{\boldsymbol{n}} H(\overline{\mathbf{U}}_{\mathrm{ax}} \cdot \widehat{\boldsymbol{n}}) \, \mathrm{dA}, \tag{3}$$

where H is the Heaviside function and $\boldsymbol{n}$ is the unit normal vector along the positive flow direction. This mean recirculating flux is then normalized by the maximum flow rate in the mother branch, $Q_{\mathrm{max}} = \pi D_0^2 \widehat{U}_{\mathrm{max}}/4$. We performed the integration defined in Eq. (3) over a series of transverse planes to quantify Q_r as a function of the distance measured along the computational domain.

The most crucial measure of recirculation from the gas transport perspective is the amount of recirculation flux that passes on to the consecutive generation, as this allows gas to be passed from
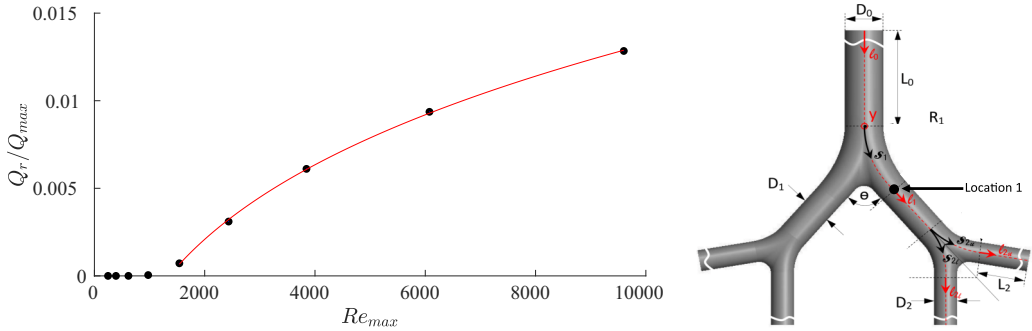
FIG. 5. Dimensionless recirculating flux computed at the borderline between the bifurcating region 1 and intermediate (daughter) branch as a function of Re_{max} for the first nine intermediate generations modeling the airway. (a) The red curve shows a power law fit for the first five intermediate generations: $Q_r = Q_{max}[0.0034(Re_{max})^{1/4} - 0.02]$. (b) The geometric location of the measurements (referred to as location 1 hereafter).

one generation to the next. To qualify mean streaming as a primary, or even significant, mechanism of gas transport in this context, the streaming needs to at least reach a few successive generation levels in the upper airway. If that is the case, the streaming flow is capable of transporting gas by virtue of a recirculation chain formed among these generation levels. In the simulation modeling the first generation of the airway, i.e., $^0G_2$, the recirculating flux measured at the boundary between the mother and daughter branch is around $0.02Q_{max}$, falling to around $0.005Q_{max}$ for the fourth generation case $^3G_5$. By the ninth generation $^8G_{10}$, the recirculating flux is effectively zero. Q_r values measured at this location (the boundary between mother and daughter branch), pertinent to the first five generation levels varies like $Re_{max}^{1/4}$ as shown in the Fig. 5(a). Figure 5(b) shows the geometric location where measurements are obtained.

Similarly, the value of Q_r measured at the borderline between the intermediate (daughter) branch and bifurcating region 2, that is, effectively the amount of recirculation flux passes on to the consecutive generation level as a function of Re_{max}, is plotted in Fig. 6(a). Notably, the amount of recirculating flux that passes on to the consecutive generation level in the $^1G_3$ case is slightly higher than that of the $^0G_2$ case despite the fact that the highest Re_{max} is associated with the latter case. Q_r
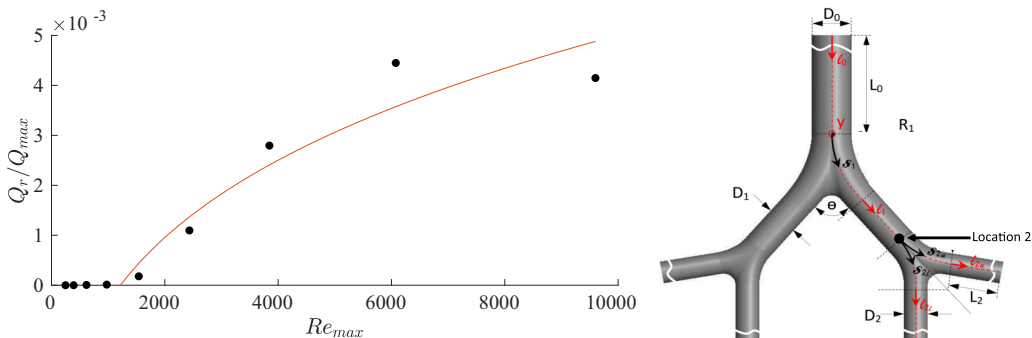

FIG. 6. Dimensionless recirculating flux computed at the borderline between the intermediate (daughter) branch and bifurcating region 2 as a function of Re_{max} for the first nine intermediate generations modeling the airway. (a) The red curve shows a power law fit for the first five intermediate generations: $Q_r = Q_{max}[0.0012(Re_{max})^{1/4} - 0.0072]$. (b) The geometric location of the measurements (referred to as location 2 hereafter).
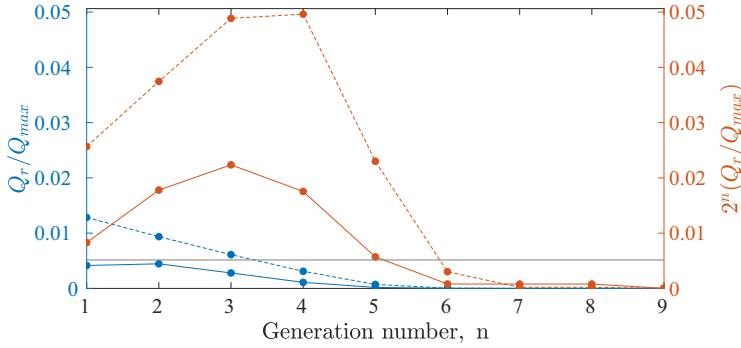
FIG. 7. Strength of the recirculating flux measured at the start and end of the intermediate generation level as a function of the generation number. Blue curves correspond to the strength of recirculating flux directly measured at a location of interest in the computational domain. Orange curves correspond to the total recirculating flux computed at each generation level. Dashed lines correspond to the measurements obtained at the borderline between the bifurcating region 1 and intermediate branch (location 1) and solid lines correspond to the measurements obtained at the borderline between the intermediate branch and bifurcating region 2 (location 2). The horizontal gray line corresponds to the flow rate required to meet the oxygen demand of a neonate in the clinical conditions based on the data reported by Hill and Robinson [42].

values measured at this location, pertinent to first five intermediate generation levels modeling the airway has been fitted to a power law of $Re_{max}^{1/4}$ as shown in the Fig. 6. There is a local maximum in the data set which is smoothed out by this fit, however, the fit still seems to capture most of the variation. Hereafter, the borderline between the bifurcating region 1 and intermediate branch is referred to as location 1 and the borderline between the intermediate branch and bifurcating region 2 is referred as location 2 for brevity.

The recirculating flux data presented in Figs. 5 and 6 can also be presented in terms of generation number. Figure 7 shows the effective strength of recirculating flux measured at the boundaries of each generation level over the first nine generations. Blue curves correspond to the strength of recirculating flux directly measured at a location of interest in the computational domain. Orange curves correspond to the total recirculating flux computed by multiplying the data in our computational domain—the blue curves—by a factor of 2^n (where n is the generation number), which represents the number of airway vessels in each generation to compute the total recirculating flux at each generation level in the airway. Dashed lines correspond to the measurements obtained at location 1 and solid lines correspond to the measurements obtained at location 2.

As shown by the orange curves, the amount of recirculating flux measured at location 1 is approximately twice that of location 2 for the first six generations. This means the strength of Q_r along a particular generation decreases by $\sim 50\%$. Q_r measured at location 1 increases from generation 1 to 4 to arrive at the highest in the generation 4, and gradually decreases in successive generations, whereas Q_r measured at location 2 increases from generation 1 to 3 to arrive at the highest in generation 3, and gradually decreases in successive generations. As a common feature for both variations, Q_r becomes negligible beyond generation 6.

The role of this streaming recirculation from the clinical perspective of HFV can be assessed by comparing it to the oxygen requirement of a patient. Assuming a oxygen demand of 7 ml kg^{-1} min^{-1} for a neonate in the clinical conditions as reported by Hill and Robinson [42], the amount of gas recirculation required to provide this can be calculated. This amount is marked by the horizontal gray line in Fig. 7. This comparison shows that the amount of oxygen passed on to the successive generation through the steady streaming phenomenon is potentially adequate to meet with the demand down to generation 5.

We note that the values of Q_r reported here are less than those we have previously reported in the single bifurcation [20]. This is due to the fact that longitudinal vortices only form downstream of a bifurcation, so in the single bifurcation case, these vortices occur in one half cycle but not the other. In the double bifurcation, there is a bifurcation at each end of the intermediate vessel, so vortices appear in both half cycles. The asymmetry between the inhalation and exhalation flow is less when longitudinal vortices are generated in both directions and is an outcome of the coupling between generations. Despite the reduction in magnitude of Q_r, the generation to which the streaming is estimated to be able to provide gas exchange that is clinically relevant is similar between the single and double bifurcation models.

The results presented here link the gas transport capacity of the streaming flow to the strength of the Dean vortices formed. This suggests a potential strategy towards the optimization of HFV and low-tidal-volume ventilation methods—finding reciprocation variations that maximize the difference between the formation of Dean vortices during inhalation and exhalation may lead to a maximum efficiency of the streaming flow to transport gas. Driving the zero-net-mass-flux flow with an optimized frequency modulation that is set up to maximize the strength of the mean flow is a potential path to optimization.

3. Instantaneous events impacting the mean structure

In Sec. I B 1, it was argued that the features observed in the streaming flow (cycle-averaged velocity) field were driven by the presence of the longitudinal vortex system generated by Dean's mechanism. Here, we further investigate the evolution of vortical structures characteristic to the flow, including how these structures become conditionally turbulent.

Concerning the $^0G_2$ case, animations |lam_0G2.avi| and |vel_0G2.avi| provided in the Supplemental Material [43] show the evolution of isosurfaces of λ_2 vortical structures and the evolution of velocity magnitude |**U**| respectively. Figure 8 shows nine panels of isosurfaces of coherent structures generated based on the λ_2 criterion, which defines vortex cores as any region where $\lambda_2 \leqslant 0$ [44]. Each panel illustrates isosurfaces of these vortical structures based on the threshold value of $\lambda_2 = -0.0025$. Three panels in the first row, Figs. 8(a1)–8(a3), correspond to isosurfaces generated based on the streaming velocity field of $^0G_2$, $^1G_3$, and $^2G_4$ cases, respectively. Similarly, three panels in the second row, Figs. 8(b1)–8(b3), correspond to isosurfaces generated based on the peak inhalation flow field of $^0G_2$, $^1G_3$, and $^2G_4$ cases, respectively. Further, three panels in the third row, Figs. 8(c1)–8(c3), correspond to isosurfaces generated based on the peak exhalation flow field of $^0G_2$, $^1G_3$, and $^2G_4$ cases, respectively.

Pertaining to the first row of Fig. 8, the streamwise vortical structures are more obvious in the $^1G_3$ case (Fig. 8(a2)) than in the $^0G_2$ case [Fig. 8(a1)]. This phenomenon seems to contradict with the variation of recirculation flux Q_r (as demonstrated in Fig. 7) where the strength of Q_r is higher in the case $^0G_2$ than that of $^1G_3$. This suggests there is a process—which we propose is conditional turbulence as demonstrated in the following sections—that destroys the coherence of the mean vortex structures in the $^0G_2$ case such that they are not reliably detected using the λ_2 criterion.

Evidence of this conditional turbulence is clear in the subsequent images in Fig. 8. The second row of images shows the λ_2 isosurfaces at peak inhalation. During the inhalation half cycle, vortical structures progressively enlarge along each daughter and granddaughter branch along the flow direction, which can be ascribed to the centrifugal instability in the curved section of each bifurcation. These structures are clear in Figs. 8(b2) and 8(b3) for the $^1G_3$ and $^2G_4$ cases, respectively. However, the $^0G_2$ case shows a much more complex structure, with the region downstream of first bifurcation being filled with small-scale turbulent eddies.

A similar process occurs during exhalation. Again, two counter-rotating vortices are formed from the centrifugal instability induced by the curvature of the bifurcation where the flow is leaving each granddaughter branch. This results in two counter-rotating vortex pairs, or four streamwise vortices, entering each daughter branch. This four-vortex system is clearly apparent in the daughter branches as shown in Fig. 8(c2) for the $^1G_3$ case. Then, this four-vortex system from each daughter

(a1) $^0G_2$, mean (a2) $^1G_3$, mean (a3) $^2G_4$, mean

(b1) $^0G_2$, Peak inhalation (b2) $^1G_3$, Peak inhalation (b3) $^2G_4$, Peak inhalation

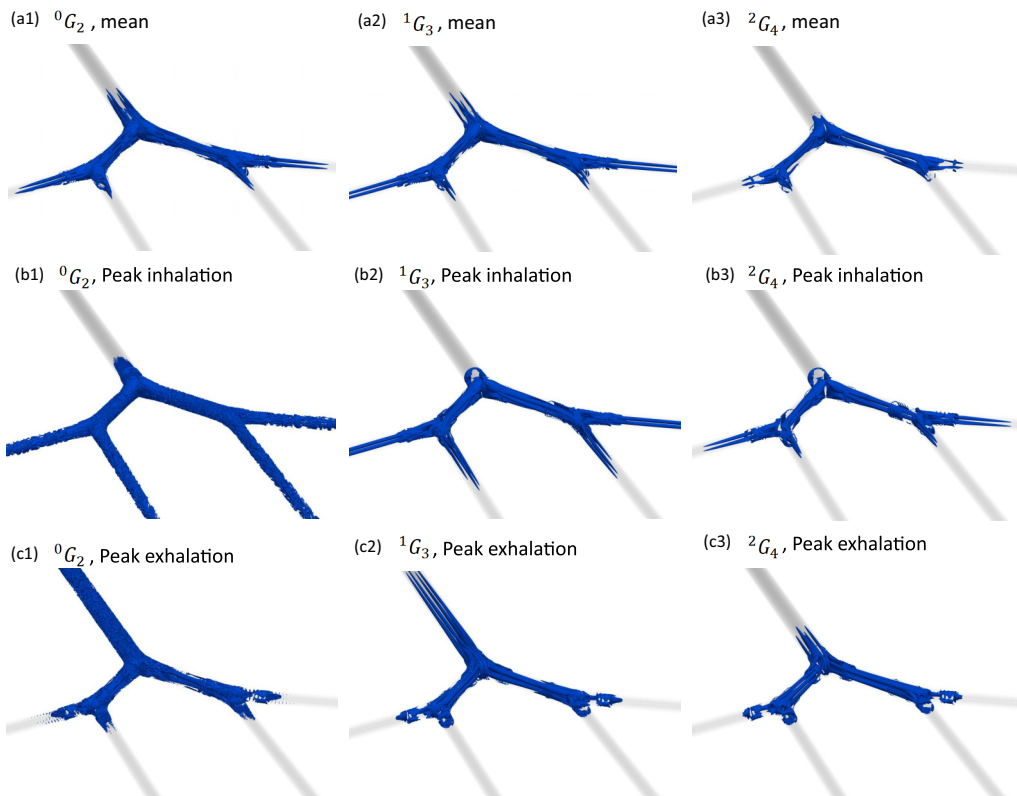(c1) $^0G_2$, Peak exhalation (c2) $^1G_3$, Peak exhalation (c3) $^2G_4$, Peak exhalation

FIG. 8. Isosurfaces of λ_2 vortical structures based on the threshold value of -0.0025. (a1), (a2), and (a3) correspond to isosurfaces generated based on the streaming velocity field of $^0G_2$, $^1G_3$, and $^2G_4$ cases, respectively. Similarly, (b1), (b2), and (b3) correspond to isosurfaces generated based on the peak inhalation flow field of $^0G_2$, $^1G_3$, and $^2G_4$ cases, respectively. Further, (c1), (c2), and (c3) correspond to isosurfaces generated based on the peak exhalation flow field of $^0G_2$, $^1G_3$, and $^2G_4$ cases, respectively. The animation |lam_0G2.avi| provided in the Supplemental Material shows the evolution of isosurfaces of λ_2 vortical structures pertinent to $^0G_2$ case.

branch enters the mother branch and becomes an eight-vortex system near the first bifurcation and rearranges to another four-vortex system away from the bifurcation. However, Fig. 8(c1) for the $^0G_2$ case shows this structure breaking down into small-scale turbulent eddies that fill the entire mother branch.

The appearance of turbulence coincides with the breakdown of the streamwise vortex structures, and we conjecture that this turbulence occurs via an instability of this vortex system. This idea is consistent with the data and we investigate the onset of this turbulent structure and its potential mechanism of generation in the following sections.

4. Instantaneous evolution of the velocity field

Here, we investigate the evolution of the instantaneous velocity field $\mathbf{u}(\mathbf{x}, t)$ over a complete flow cycle, focusing on the $^0G_2$ and $^1G_3$ cases, which have the highest Reynolds numbers and are therefore the most susceptible for turbulence. Results are presented here at 12 instants and for clarity and conciseness of flow visualizations, only one-half of the fluid domain is shown in each panel. These velocity fields were indeed verified to be statistically symmetric around the z axis, reflecting the symmetry of the local geometry. The overall conclusions of this section are similar to those from our study of a single bifurcation [20]. There are some important differences, however,
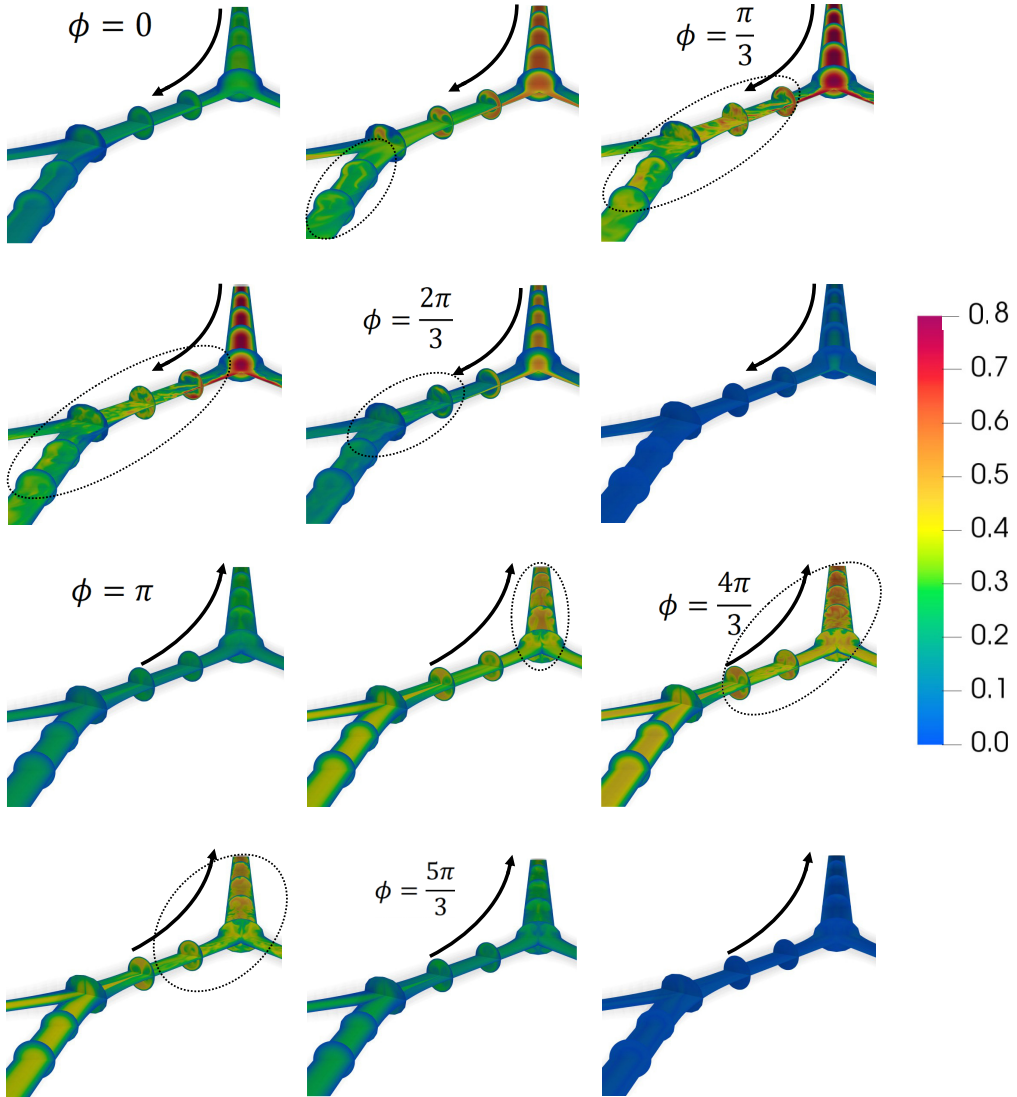
FIG. 9. Evolution of the instantaneous velocity magnitude, $|\mathbf{U}|$ for $^0G_2$ ($\mathrm{Re}_{\max} = 9600$, $\alpha = 3.36$). The dotted lines highlight areas where turbulent bursts have developed in the flow. The animation |vel_0G2.avi| provided in the Supplemental Material shows the evolution of $|\mathbf{U}|$.

regarding which cases (i.e., at which value of $\mathrm{Re}_{\max}$) become turbulent, that indicate the presence of turbulence can be influenced by changes in upstream *and* downstream conditions.

Figures 9 and 10 show contours of velocity magnitude $|\mathbf{U}|$ for 12 consecutive phases of the cycle among cases $^0G_2$ and $^1G_3$. The first and last panels correspond to $\phi = 0$ and $\phi = \frac{11}{6}\pi$, respectively, with an interval of phase angle $\Delta\phi = \frac{\pi}{6}$ between each consecutive panel. The upper six panels of each figure corresponds to the inhalation half cycle while the lower six panels correspond to exhalation.

For the $^0G_2$ case, during the first quarter of the cycle (acceleration phase during which the inhalation flow rate increases with time), a high momentum region progressively develops in the core of the mother branch and propagates along the inner walls of the daughter branches.
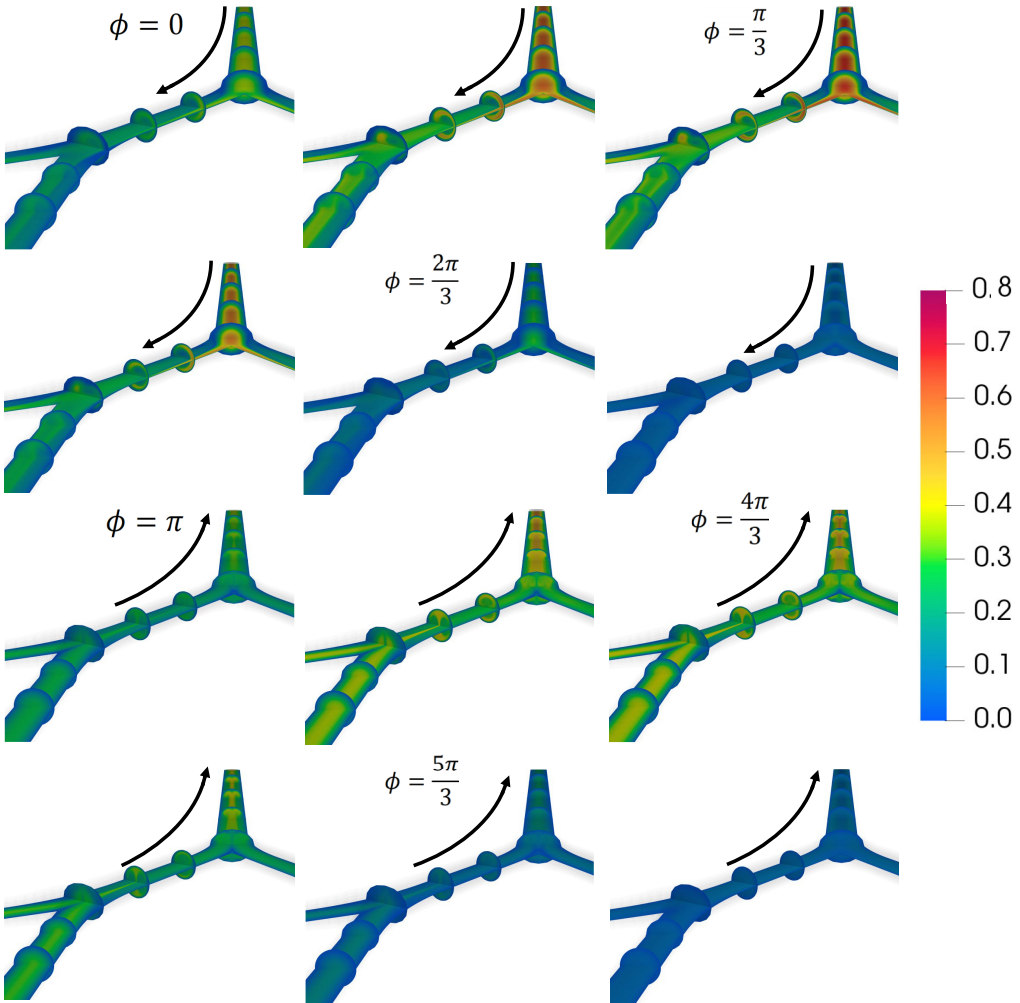
FIG. 10. Evolution of the instantaneous velocity magnitude, $|\mathbf{U}|$ for $^1G_3$ ($\mathrm{Re_{max}} = 6076$, $\alpha = 2.66$).

Simultaneously, slightly weaker high momentum regions evolve in the core of daughter branches and propagate downstream along the inner walls of the granddaughter branches. Near the bifurcating regions, these high momentum regions progressively contrast with the slower moving air at the outer wall. The stronger high momentum region developed at the inner walls of the daughter branches breaks down to turbulence, approximately from $1.2D_1$, measured along the daughter branches (from the origin of the first bifurcation) when $\phi = \pi/3$. This turbulence rapidly convects downstream and appears to be sustained for $\frac{\pi}{3} \leqslant \phi \leqslant \frac{2\pi}{3}$ as depicted from Fig. 9. This turbulence is also sustained in the granddaughter branches.

In the second quarter of the cycle (deceleration phase during which the inhalation flow rate decreases with time), the turbulence decays when the flow velocity decreases below a critical value. Eventually, the high momentum region depletes and the flow relaminarizes as shown in $\frac{2\pi}{3} \leqslant \phi \leqslant \frac{5\pi}{6}$. At $\phi = \frac{5\pi}{6}$, the flow velocity decreases to zero before alternating direction between inhalation and exhalation phases.

In the third quarter of the cycle (acceleration phase during which the exhalation flow rate increases with time), the flow progresses from granddaughter to daughter and daughter to mother

branches. These flows merge to create jetlike high-momentum regions and these high-momentum regions propagate along the core of the daughter and mother branches. As depicted from Fig. 9, at $\phi = \frac{7\pi}{6}$, the high-momentum region formed along the core of the mother branch breaks down to turbulence, approximately from $5D_0$ measured along the mother branch. Simultaneously, jetlike high-momentum regions formed along the core of the daughter branches undergo an instability, leading to approximately periodic pulses that convect along the flow (this periodic pulsing is clear in the animation |vel_0G2.avi| provided in the Supplemental Material). This pulsing process repeats 15 times during an epoch around the peak exhalation flow rate and appears to cause the generation of turbulence in the daughter branches. This turbulence, however, is not sustained and disappears immediately once the pulse is convected. The discrete nature of the flow instability generated here differentiates it from the classical fully developed turbulence.

In the final quarter of the cycle (deceleration phase during which the exhalation flow rate decreases with time), the turbulence decays in both daughter and mother branches and the flow relaminarizes while the high momentum region depletes gradually to facilitate the flow inversion for the next cycle.

A comparison of Figs. 9 and 10 reveals that the corresponding cases $^0G_2$ and $^1G_3$ share qualitatively similar basic flow features except that there is no turbulence observed in the latter case. This is despite the fact that there is a correspondence between the bulk flow conditions in different sections of each case, i.e., Re_{max} and α in the daughter branch of the $^0G_2$ case are the same as in the mother branch of the $^1G_3$ case. We also note that a single-bifurcation case with the same Re_{max} and α as the $^1G_3$ case (i.e., a $^1G_2$ case) presented in our previous study [20] displayed turbulence during exhalation. There is an influence of geometry on the development of turbulence, and this is further investigated in Sec. I B 5.

The results here confirm that the basic mechanism for the development of turbulence is the same as in the single bifurcation case [20], where turbulence stems from an instability of the streamwise Dean vortices generated as the flow passes through the curved sections of the bifurcation, once a critical value of flow rate is exceeded.

Figure 11 shows time traces of the axial velocity $\mathbf{U}_{ax}$ at the geometric center of each generation (center of the cross sections A-A′, B-B′, C-C′, and D-D′ of Fig. 4). Three curves are shown in each panel: the raw history of $\mathbf{U}_{ax}$ is shown in black, the low-pass filtered $\mathbf{U}_{ax}$ is shown in green, and high-pass filtered $\mathbf{U}_{ax}$ is shown in red, using a cutoff frequency of $f_{thr}D_0/\widehat{U}_{max} = 0.05$ (note the frequency of the cycle for $^0G_2$ case is $fD_0/\widehat{U}_{max} = 2\alpha^2/(\pi\mathrm{Re}_{max}) = 7.5 \times 10^{-4}$). This decomposition enables the quantification of the time duration for which turbulence prevails.

Figure 11 reveals the appearance of turbulent bursts at times near maximum flow rate in either direction and in portions of the cycle where streamwise vortices are present (only during exhalation in the mother branch, only during inhalation in the granddaughter branches, and during both inhalation and exhalation in the daughter branch). We reaffirm the conclusion we reported for the single bifurcation in Jacob *et al.* [20]; this breakdown to turbulence is distinctly different from the process in a straight tube in which the turbulent bursts typically occur at epochs centered around the peak deceleration [22,23]. The presence of curvature leading to Dean vortices is crucial to the breakdown process in the bifurcation geometry.

Figure 11(b) also shows evidence of the periodic bursting process that occurs in the daughter branch during exhalation. Further stability analysis is warranted to completely understand this phenomenon.

5. *Effect of upstream and downstream conditions on the development of turbulence*

The previous sections have shown that the basic scenario for the appearance of conditional turbulence in the double bifurcation is similar to that uncovered in the single bifurcation reported in Jacob *et al.* [20], where turbulence occurs as a function of the local, and instantaneous, Reynolds number. However, the data of the present paper allows this appearance to be studied in more detail
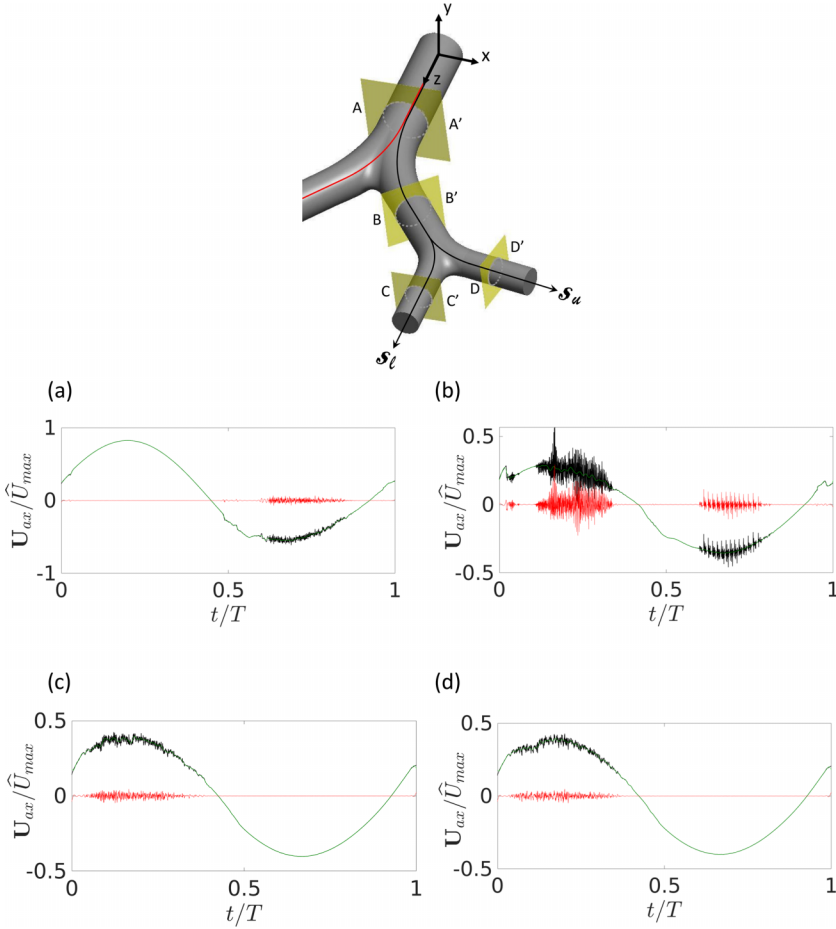
FIG. 11. A decomposition of the time history of axial velocity $\mathbf{U}_{ax}$ of the ${}^{0}G_2$ case. (a) Decomposition of temporal axial velocity ($\mathbf{U}_{ax}$) at the center of the cross section A-A′. (b) Decomposition of temporal axial velocity ($\mathbf{U}_{ax}$) at the center of the cross section B-B′. (c) Decomposition of temporal axial velocity ($\mathbf{U}_{ax}$) at the center of the cross section C-C′. (d) Decomposition of temporal axial velocity ($\mathbf{U}_{ax}$) at the center of the cross section D-D′. These cross sections are shown in Fig. 4. Solid black line shows the measured temporal data from the instantaneous velocity field; solid green line shows the velocity scale associated with the filtered low-frequency components while the solid red line shows the velocity scale associated with the filtered high-frequency components. The cutoff frequency for the low- and high-pass filters was $f_{thr}D_0/\widehat{U}_{max} = 0.05$.

by comparing flows with the same local and instantaneous parameters, but differing upstream and downstream conditions.

In this section, we interrogate various simulation cases with equivalent local and instantaneous conditions, i.e., the same Reynolds and Womersley numbers, but different upstream and downstream conditions. For instance, the reciprocating flow through the lower bifurcating junctions of the ${}^{0}G_2$ case (the two junctions between G_1 and G_2) shares the same local Reynolds number and Womersley number combination with the flow through the upper bifurcating junction of the ${}^{1}G_3$ case (the junction between $G1$ and $G2$); however, they correspond to different upstream and downstream conditions.

In fact, this comparison (lower junctions of the ${}^{0}G_2$ case with the upper junction of the ${}^{1}G_3$ case) can be made qualitatively from the flow visualisations of the ${}^{0}G_2$ case in Fig. 9 the ${}^{1}G_3$ case in

Fig. 10—it is clear that the flow characteristics during the inhalation are dependent on the upstream conditions. The lower bifurcating junctions of the $^0G_2$ case see turbulent bursts during an epoch centered around peak inhalation flow rate, while the upper bifurcating junction of the $^1G_3$ case does not see such bursts. Apparently, the production of turbulence upstream is destabilising downstream and this turbulence is convected and sustained into the lower generations.

This observation is further quantitatively examined by plotting the temporal variation of axial velocity $\mathbf{U}_{ax}$ of the $^1G_3$ case in Fig. 12, sampled on the centreline in each generation. The locations of the sampling are in a geometrically similar position to those used for the sampled velocity data for the $^0G_2$ case shown in Fig. 11.

So, the sample location B-B′ and the local Reynolds and Womersley numbers at this location in the $^0G_2$ case are equivalent to location A-A′ in the $^1G_3$ case (the same equivalence occurs for C-C′/D-D′ in the $^0G_2$ case and B-B′ in the $^1G_3$ case). Therefore, Figs. 11(b) and 11(d) can be compared with Figs. 12(a) and 12(b)—the data have been sampled at geometrically similar locations, and the bulk flow conditions are also similar. Such a comparison reveals significant differences in the time history of axial velocity $\mathbf{U}_{ax}$, which can be ascribed to the differences in upstream *and* downstream conditions among these cases.

The impact of this coupling between upstream and downstream generations is further investigated by comparing the cases described above to the flow in an isolated 1:2 bifurcation which, by design, removes the intergeneration coupling. Again, geometric and bulk dynamic similarity is maintained. Further, the computational mesh of each bifurcation employed is identical—the multigeneration meshes are constructed by connecting single generation meshes, thereby removing mesh dependence as a reason for any difference between the results from each simulation. The corresponding temporal evolution of axial velocity $\mathbf{U}_{ax}$ is shown in Fig. 13.

The velocity traces produced are different from those from the multigeneration simulations shown in Figs. 11 and 12 for both the inhalation and exhalation flow. For example, Fig. 11(b) with the lower left panel of Fig. 13 compare the velocity trace in vessel generation 1 (the vessel beyond the first bifurcation) for the multigeneration and single generation cases, respectively, with the same Reynolds and Womersley numbers in the mother branch. During inhalation, the only difference is the conditions downstream of the measurement point—the multigeneration mesh has another bifurcation, the single generation mesh has a long straight section. The velocity trace over the inhalation period ($t/T < 0.5$) is similar in that turbulence occurs near the peak flow rate, however, the amplitude of this turbulent fluctuation is clearly larger in the multigeneration case.

An important conclusion of this comparison is that it is not only *upstream* conditions that impact the production of turbulence; *downstream* conditions also need to be considered. We also highlight that the upstream and downstream directions reverse as the cycle moves from inhalation to exhalation.

This dependence on upstream and downstream conditions is further highlighted by visualizing the flow passing through each vessel generation for various setups. Figure 14 shows the setups used and the locations of planes used for comparative visualisation. The evolution of the instantaneous velocity magnitude, $|\mathbf{U}|$ among cases with equal Reynolds and Womersley numbers, is shown on these planes in Fig. 15. Figures 15(a1) and 15(a2) correspond to cross sections located at the geometric center of the mother branch of the *single* bifurcation $^1G_2$ case and the left daughter branch (section B-B′ of Fig. 4) of the *double* bifurcation $^0G_2$ case, respectively. Figures 15(b1) and 15(b2) correspond to the left daughter branch of the *single* bifurcation $^1G_2$ case and the upper left granddaughter branch (section D-D′ of Fig. 4) of the *double* bifurcation $^0G_2$ case, respectively. Each row contains 12 consecutive phases of the cycle and the first and last panels correspond to $\phi = 0$ and $\phi = \frac{11}{6}\pi$, respectively, with an interval of phase angle $\Delta\phi = \frac{\pi}{6}$ between each consecutive panel. The first six panels of each row correspond to the inhalation half cycle while the second six panels correspond to exhalation.

Figure 15(a1) shows images from the first (mother) generation vessel of a single generation $^1G_2$ case, whereas Fig. 15(a2) are taken from the intermediate generation vessel of a multigeneration $^0G_2$ case.
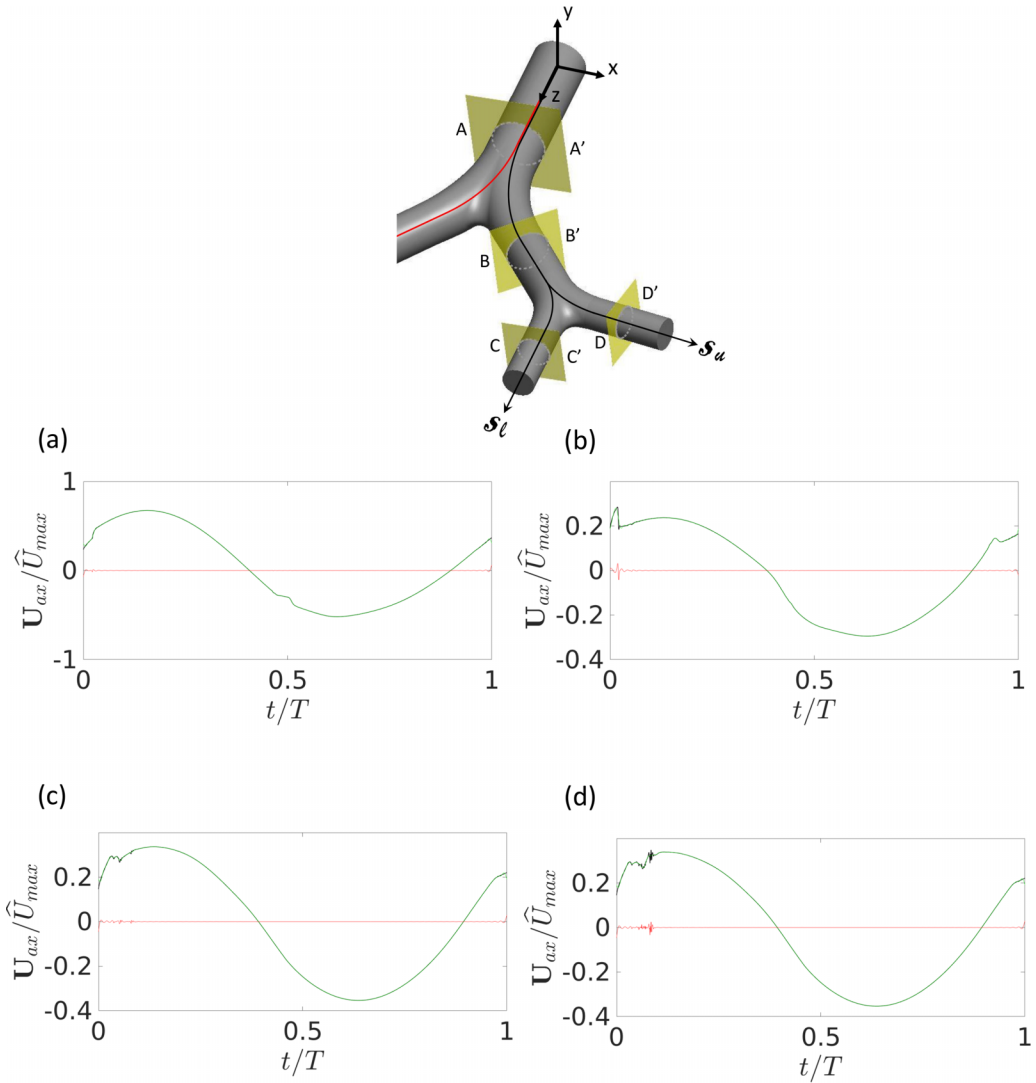
FIG. 12. A decomposition of the time history of axial velocity $\mathbf{U}_{ax}$ of the $^1G_3$ case. (a) Decomposition of temporal axial velocity ($\mathbf{U}_{ax}$) at the center of the cross section A-A′. (b) Decomposition of temporal axial velocity ($\mathbf{U}_{ax}$) at the center of the cross section B-B′. (c) Decomposition of temporal axial velocity ($\mathbf{U}_{ax}$) at the center of the cross section C-C′. (d) Decomposition of temporal axial velocity ($\mathbf{U}_{ax}$) at the center of the cross section D-D′. Solid black line shows the measured temporal data from the instantaneous velocity field; solid green line shows the velocity scale associated with the filtered low-frequency components while the solid red line shows the velocity scale associated with the filtered high-frequency components. The cutoff frequency for the low- and high-pass filters was $f_{thr}D_0/\widehat{U}_{max} = 0.05$.

The upstream conditions during the inhalation period [shown in the first six images of Figs. 15(a1) and 15(a2)] differ. The flow in the multigeneration case has already passed through a bifurcation, generating Dean vortices that subsequently become turbulent. The flow in the single generation case has only traversed the straight pipe section and presents an axisymmetric velocity profile. This strong modification by the upstream curvature is not surprising.
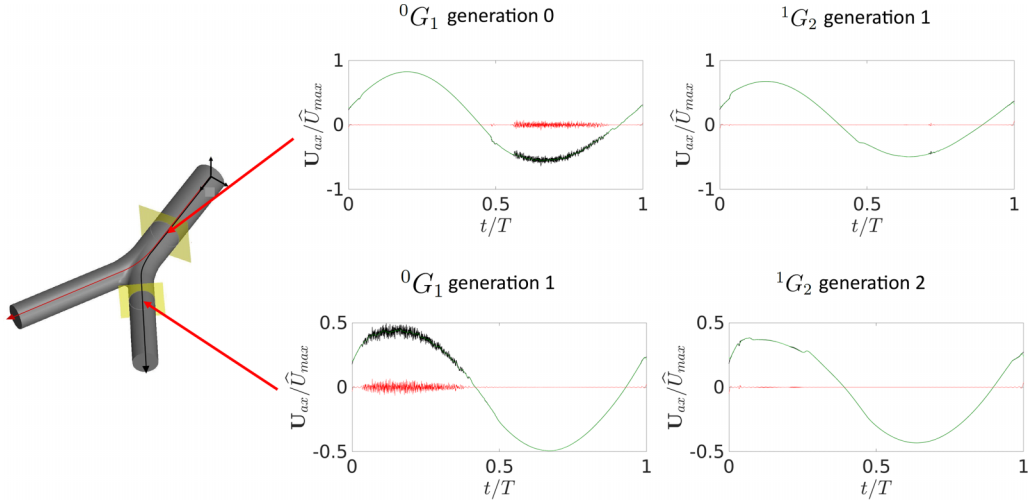
FIG. 13. A decomposition of the time history of axial velocity $\mathbf{U}_{ax}$ of the *single* bifurcation $^0G_1$ and $^1G_2$ cases. $^0G_1$ generation 0: Decomposition of $\mathbf{U}_{ax}$ at the geometric center of the mother branch of $^0G_1$ case. $^0G_1$ generation 1: Decomposition of $\mathbf{U}_{ax}$ at the geometric center of a daughter branch of $^0G_1$ case. $^1G_2$ generation 1: Decomposition of $\mathbf{U}_{ax}$ at the geometric center of the mother branch of $^1G_2$ case. $^1G_2$ generation 2: Decomposition of $\mathbf{U}_{ax}$ at the geometric center of a daughter branch of $^1G_2$ case. Solid black line shows the measured temporal data from the instantaneous velocity field; solid green line shows the velocity scale associated with the filtered low-frequency components, while the solid red line shows the velocity scale associated with the filtered high-frequency components. The cutoff frequency for the low- and high-pass filters was $f_{thr}D_0/\widehat{U}_{max} = 0.05$.

The comparison of the exhalation period [shown in the second six images of Figs. 15(a1) and 15(a2)] is less intuitive. During this exhalation period, the flow in the vessel shown is supplied by a flow that has passed through one bifurcation in both cases. All that changes is the downstream conditions—in the multigeneration case the vessel merges with another through a second bifurcation, whereas in the single generation case the vessel continues in a straight path. The images show there is a significant difference in the flow generated. Notably, the multigeneration case displays a turbulent (or at least a spatiotemporally complex) flow when the flow rate is maximum near $\phi = 4\pi/3$, whereas the single generation case shows well-defined vortices throughout the exhalation period. The apparent conclusion is that the development of turbulence in this vessel is linked to the change in downstream conditions.

Figures 15(b1) and 15(b2) show the flow at a location in the vessel at generation 2: Fig. 15(b1) shows a cross section in the daughter branch of the single generation $^1G_2$ case, whereas Fig. 15(b2) shows a cross section in the granddaughter branch of the multigeneration $^0G_2$ case.

The first six panels of Figs. 15(b1) and 15(b2) correspond to inhalation, and so the upstream conditions between the two cases vary. Again, the flows are somewhat different to each other—the combined effects of curvature and flow division at multiple bifurcating junctions in the multigeneration case accumulate. The Dean vortices produced in the vessel at generation 1 have some impact on the Dean vortices produced in the vessel at generation 2, however, the basic flow structure still appears to be dictated by these Dean vortices.

The second six panels of Figs. 15(b1) and 15(b2) correspond to exhalation, so only the downstream conditions vary. The flows generated in this case are qualitatively similar, the axisymmetric velocity profiles generated through the straight inlet section of pipe do not appear to be impacted by the downstream conditions.
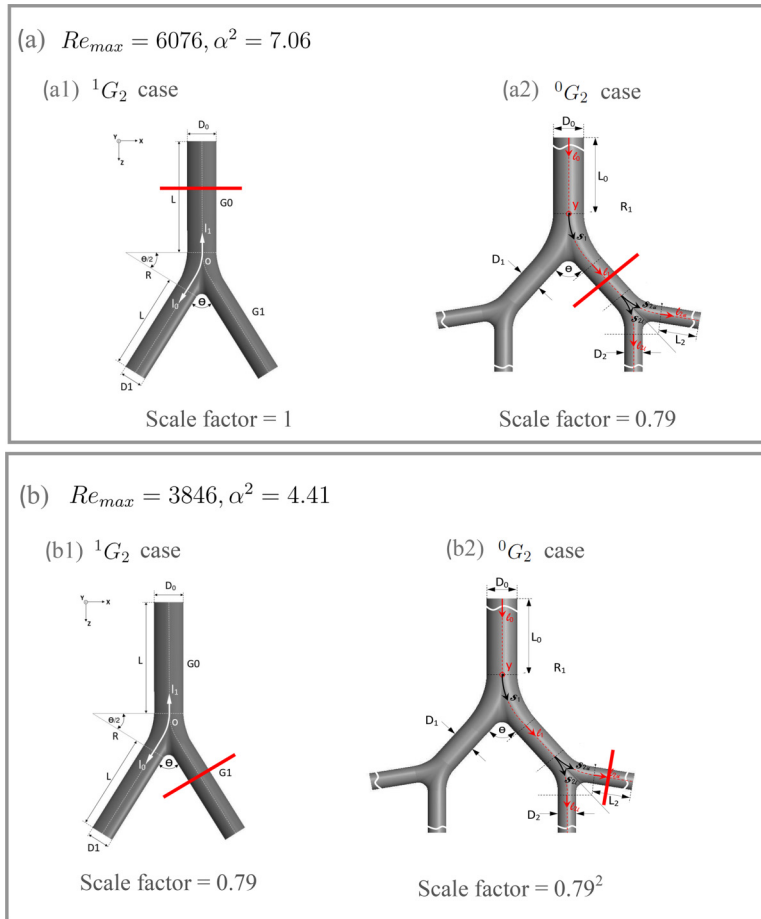
FIG. 14. Geometric locations compared in various simulation configurations shown in Fig. 15. (a1), (a2), (b1), and (b2) are dynamically equivalent location pairs located at the geometric center of the mother branch of $^{1}G_2$ case, the left daughter branch (section B-B$'$ of Fig. 4) of $^{0}G_2$ case, the left daughter branch of $^{1}G_2$ case, and the upper left granddaughter branch (section D-D$'$ of Fig. 4) of $^{0}G_1$ case, respectively. The scaling factors used to scale up each cross section to make them identical are shown.

Taken together, one intuitive conclusion is that the development of turbulence is a strong function of the upstream conditions. Considering the fact that a preceding bifurcation generates a flow containing Dean vortices and a strong secondary flow (i.e., the flow normal to the axis of the vessel), whereas the flow in a straight section is purely parallel, this outcome is not surprising.

What is less intuitive is the dependence on downstream conditions that is not universal—for example, the comparison of the exhalation flow in the vessel at generation 2 showed no dependence on upstream conditions during exhalation, whereas the flow in the vessel at generation 1 does show a dependence. This is possibly linked to the flow being supplied—the flow compared in generation 2 is essentially axisymmetric, whereas that compared at generation 1 contains Dean vortices. It is possible that the deficit produced by the Dean vortices and secondary flow provide a feedback mechanism, allowing the disturbance to the flow introduced by the second downstream bifurcation to be communicated upstream and therefore destabilize the flow. Such a feedback mechanism is not present in the purely parallel flow.
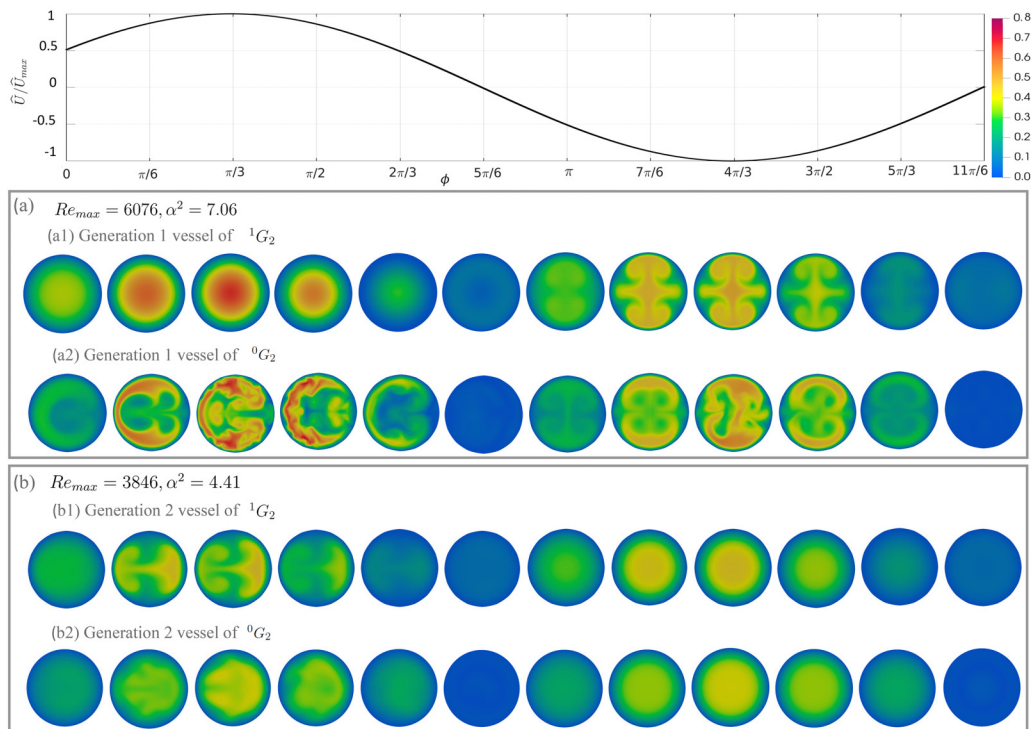
FIG. 15. A comparison of the evolution of the instantaneous velocity magnitude, $|\mathbf{U}|$, among dynamically equivalent flow configurations shown in Fig. 14. Rows (a1), (a2), (b1), and (b2) display 12 snapshots of $|\mathbf{U}|$ at cross sections located at the geometric center of the mother branch of ${}^1G_2$ case, the left daughter branch (section B-B$'$ of Fig. 4) of ${}^0G_2$ case, the left daughter branch of ${}^1G_2$ case, and the upper left granddaughter branch (section D-D$'$ of Fig. 4) of ${}^0G_1$ case, respectively. Note that the diameter of daughter and granddaughter branches are scaled up by a factor of 0.79 and 0.79^2 to make them identical for comparison purposes. The top panel shows the variation of flow rate as a function of time.

A more formal stability and sensitivity analysis of the flow is required to completely establish this link, which we will pursue in a future study. What is clear is that the generation of turbulence in the airway is not a completely "local" phenomenon, and that generational coupling needs to be considered in both the upstream and downstream directions if the impact of turbulence is to be understood.

C. CONCLUSION

The aim of the present paper is to quantify the nonlinear mean streaming and the generation of turbulence in the reciprocating flow in a double bifurcation as a model flow for that in the human airway during HFV.

The mean streaming measured in the double bifurcation is around 2% of the maximum flow rate, which is less than the $\sim 5\%$ we have previously reported in the single bifurcation [20]. The reduction can be ascribed to the intergeneration coupling effects. However, these results suggest that the amount of oxygen supplied through this phenomenon likely meets the anticipated oxygen demand of a neonate in the first five generations of the airway.

As an important feature of the reciprocating flow, turbulent bursts are observed in the first three generations of the airway when the flow speed exceeds a critical value. The flow relaminarizes periodically when the flow speed decreases below the critical value. However, the results of
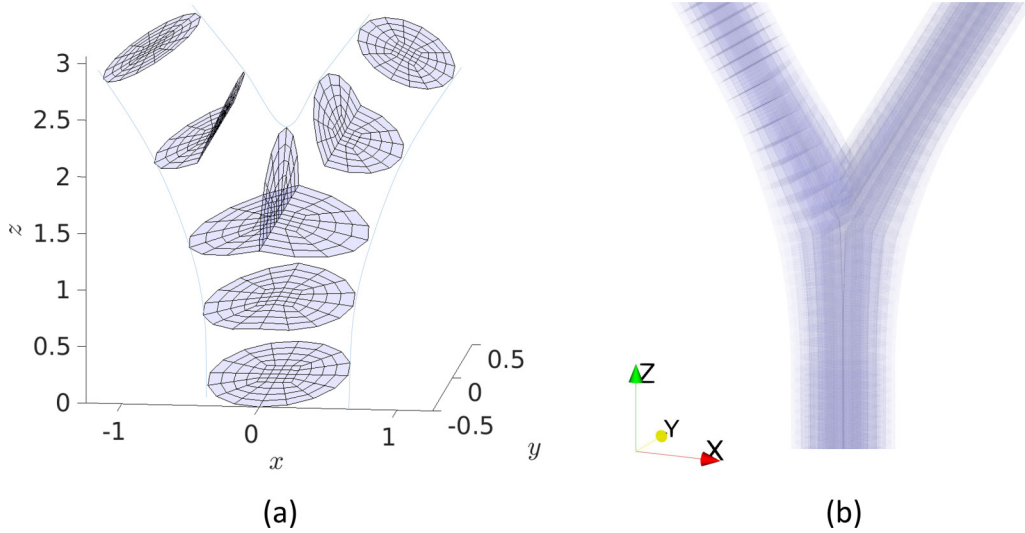
FIG. 16. The mesh topology of a bifurcating junction used in the study. (a) Macro mesh topology of a bifurcating junction. (b) Resulting mesh topology of hexahedral elements associated with Gauss-Legendre-Lobatto quadrature points of eighth-order tensor-product Lagrange polynomials.

this paper show that this critical value is a function of the geometry. The onset, advection, and sustenance of turbulence in a given vessel appears to be a function of the upstream and *downstream* flow conditions. Multiple generations of the airway must be considered to fully understand this phenomenon.

ACKNOWLEDGMENTS

APPENDIX: MESH RESOLUTION TESTS

Mesh resolution tests were conducted to ensure the dynamics were correctly resolved, especially for the turbulent cases. Both local and global parameters were monitored as a function of spatial resolution to determine an optimal spatial resolution for each flow regime. Generally, the spatial resolution of spectral element simulations is changed by varying the interpolation polynomial order (*p* refinement) or varying the number of elements in the macro mesh (*h* refinement). When these two refinement approaches are coupled, it leads to a hybrid method known as *h-p* method [45]. However, for the simplicity of implementation, varying the interpolation polynomial order (*p* refinement) was adopted here, while keeping the macromesh layout the same. The macrostructure of the mesh employed in each bifurcation is shown in Fig. 16.

The evolution of axial velocity component $\mathbf{U}_{ax}$ measured at the geometric center of generation 1 (the intermediate generation coupled by upstream and downstream generations) was chosen to be the local parameter and energy norm was chosen to be the global parameter. Note that the energy norm is equivalent to the ensemble average of root-mean-squared velocity. Global parameters are
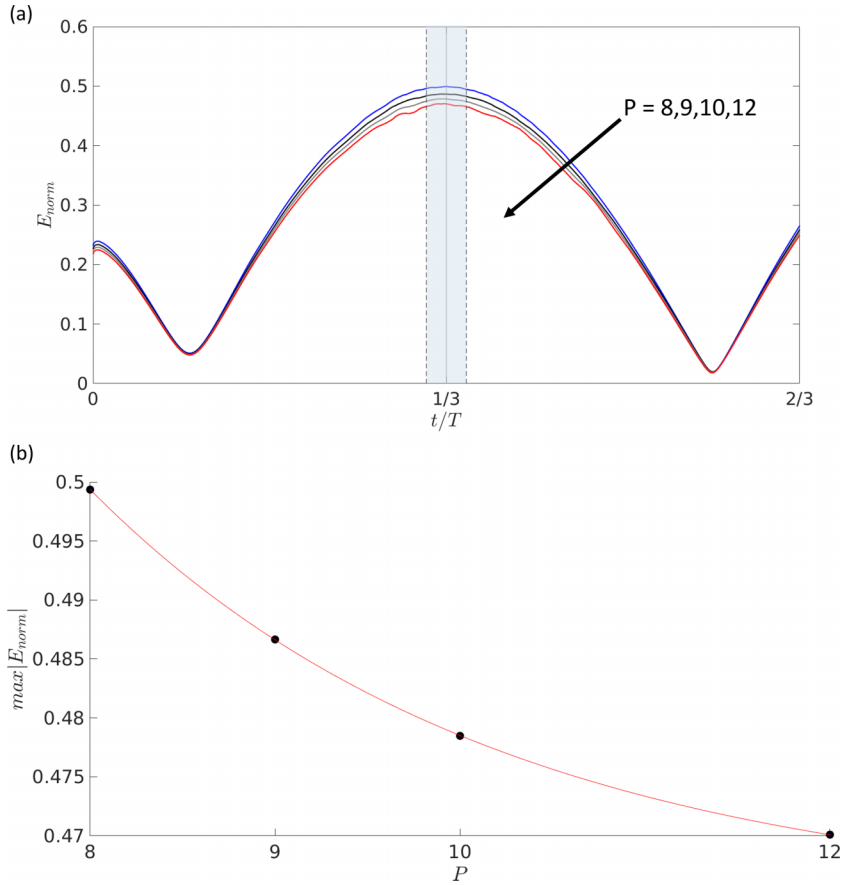
FIG. 17. The variation of energy norm (E_{norm}) as the global indicator of convergence. (a) The temporal evolution of E_{norm} over a portion of the reciprocating flow cycle, i.e., $0 \leqslant t \leqslant \frac{2T}{3}$, where T is the reciprocation period; for varying interpolation polynomial order, i.e., $P = 8, 9, 10, 12$. (b) The variation of maximum energy norm $\max|E_{norm}|$ as a function of interpolation polynomial order P. The red curve shows an exponential convergence of $\max|E_{norm}|$ as a function of P: $\max|E_{norm}| = 0.464 + \frac{1.216}{e^{0.441P}}$.

sensitive to the changes in the entire domain as their computation accounts for all the grid points in the domain securing the spectral accuracy.

The macromesh layout shown in Fig. 16 was used throughout the test with varying interpolation polynomial order ($P = 8, 9, 10, 12$), resulting in meshes of different spatial resolutions. The evolution of energy norm was monitored as the global indicator of convergence over a portion of the reciprocating flow cycle ($0 \leqslant t \leqslant \frac{2T}{3}$, where T is the reciprocation period) for varying interpolation polynomial order ($P = 8, 9, 10, 12$) and presented in Fig. 17.

It is evident from Fig. 17(a) that the curves representing the evolution of E_{norm} for varying P are coincident with each other at the minimum flow rates. However, they show a discrepancy at the maximum flow rate where the flow is unsteady and turbulent. They correspond to a percentage discrepancy of 4.3% between $P = 8$ and $P = 12$. A clear trend of decreasing E_{norm} with increasing P is observed at higher flow rates and this can be ascribed to the introduction of more and more (small) dissipative scales to the simulation. According to the Kolmogorov hypothesis, the turbulent kinetic energy dissipation of a viscous fluid flow takes place at a small scale known as the Kolmogorov scale [46]. The smallest grid spacing of a mesh should be less than the Kolmogorov scale for a given mesh to fully resolve the flow including these dissipative scales. The finer the mesh spacing
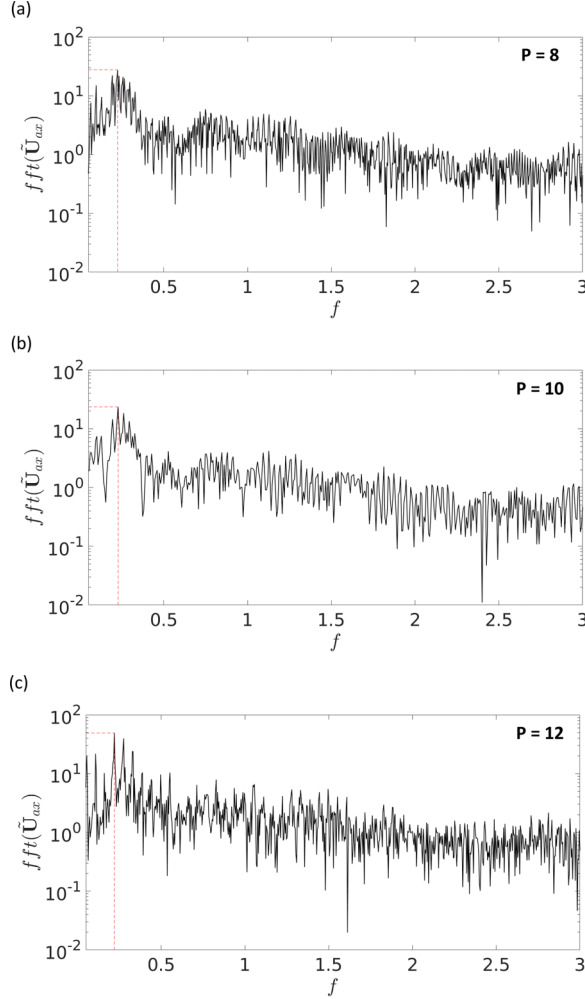
(a)

(b)

(c)

FIG. 18. Frequency spectrum of the instantaneous axial (streamwise) velocity $\mathbf{U}_{ax}$ time history. (a)–(c) Frequency spectrum of the $\mathbf{U}_{ax}$ time history measured at the geometric center of generation 1 (geometric center of section B-B′) for $P = 8, 10, 12$. The cutoff frequency for the high-pass filter was $f_{thr}D_0/\widehat{U}_{max} = 0.05$. The peak dimensionless oscillation frequency $f_{max}D_0/\widehat{U}_{max}$ is marked with a red dashed line.

or higher the spatial resolution, the capability of resolving for these dissipative scales increases. Consequently, the energy norm decreases with the increasing spatial resolution (increasing P order) and converges to a fixed value.

The maximum energy norm ($\max|E_{norm}|$) of each interpolation polynomial order (P) corresponds to the grey vertical line of Fig. 17(a) and plotted in Fig. 17(b). The variation of $\max|E_{norm}|$ as a function of P is given by the below exponential fit,

$$\max|E_{norm}| = 0.464 + \frac{1.216}{e^{0.441P}}, \tag{A1}$$

and shown by the red curve. This means that an exponential convergence of energy norm (used as a global convergence indicator) can be achieved by increasing the interpolation polynomial order. This shows that as $P \to \infty$, $\max|E_{norm}| \to 0.464$ and further indicates that the variation of $\max|E_{norm}|$ for $P = 12$ is within 5% of the converged value.
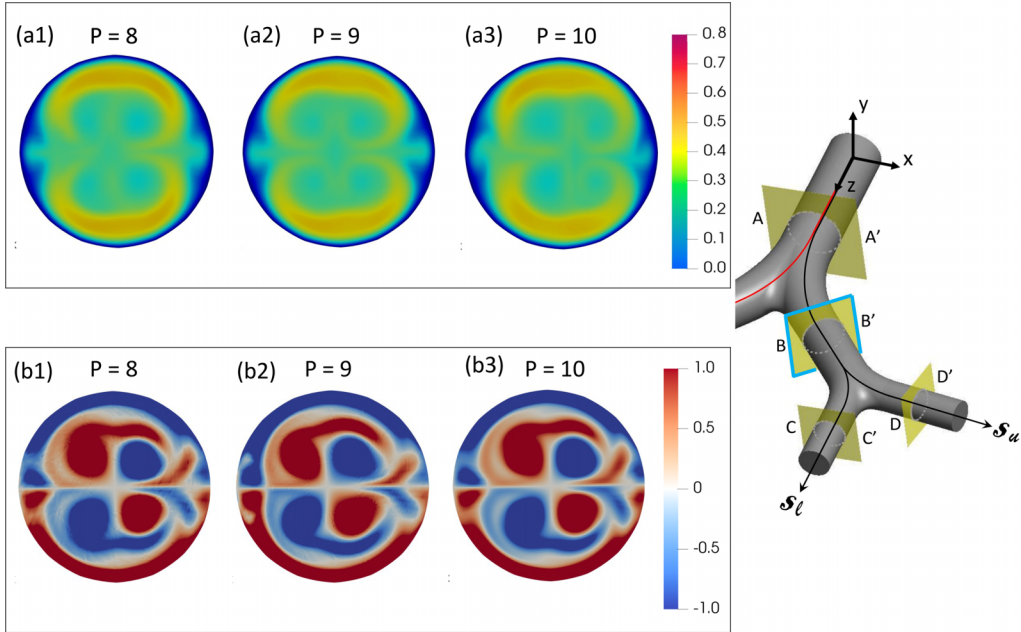
FIG. 19. A comparison of instantaneous velocity magnitude $|\mathbf{U}|$ and instantaneous axial vorticity ω_{ax} at the peak flow rate indicated by the vertical grey line of Fig. 17(a) for varying interpolation polynomial order (P). (a1)–(a3) Snapshots of $|\mathbf{U}|$ at the peak flow rate for $P = 8, 9, 10$, respectively. (b1)–(b3) Snapshots of ω_{ax} at the peak flow rate for $P = 8, 9, 10$, respectively. All the snapshots are taken from the vertical plane passing through the geometric center of generation 1 (section B-B′).

The grid convergence properties near the peak flow rate (where the discrepancy of $\max|E_{norm}|$ is observed and the flow is most likely to be turbulent) were further investigated by considering the frequency spectrum of the time history of instantaneous axial (streamwise) velocity $\mathbf{U}_{ax}$ in the shaded region of Fig. 17(a). The frequency spectrum near the peak flow rate pertaining to each polynomial order is shown in Fig. 18 and the primary frequency observed in the spectrum is annotated in each polynomial order case.

This spectrum is formed from the Fourier transform of the time history of the axial velocity measured at the geometric center of generation 1 (geometric center of section B-B′) for each polynomial order over the shaded region shown in Fig. 17(a). The peak frequencies observed in the spectrum for $P = 8, 10, 12$ are $f_{max}D_0/\widehat{U}_{max} = 0.220, 0.224, 0.226$, respectively. The frequency spectra are not identical—however, they share many qualitative similarities and the peak frequencies are nearly identical. This leads to the hypothesis that the polynomial order $P = 12$ is capable of capturing the essential physics of the flow.

Having investigated global and local quantitative measures of grid convergence, a local but qualitative indicator is interrogated here. Snapshots of velocity magnitude $|\mathbf{U}|$ and axial vorticity ω_{ax} for varying interpolation polynomial order (P) are visualized and compared at the peak flow rate indicated by the vertical grey line of Fig. 17(a).

Snapshots of $|\mathbf{U}|$ and ω_{ax} shown in Fig. 19 share qualitatively similar flow structures. Note that section B-B′ of Fig. 1(b) is visualized here. These visualizations share qualitatively similar primary features, particularly the location and size of the vortices and shear layers. However, some underresolved regions are observed in ω_{ax} contours pertaining to high-velocity gradients. This under-resolved nature decreases with increasing interpolation polynomial order P and almost disappears at $P = 10$. As further evidence from this flow visualization, it is preferable to have higher $P(\geqslant 10)$ in terms of accuracy and hence $P = 12$ is used for simulation cases that are likely to be

turbulent. Therefore, it can be safely concluded that the interpolation polynomial order $P = 12$ is capable of capturing the essential physics of the reciprocating flow.

---

[1] T. Standiford and M. Morganroth, High-frequency ventilation, Chest **96**, 1380 (1989).

[2] K. Bauer, E. Nof, and J. Sznitman, Revisiting high-frequency oscillatory ventilation in vitro and in silico in neonatal conductive airways, Clin. Biomech. **66**, 50 (2019).

[3] H. Chang, Mechanisms of gas transport during ventilation by high-frequency oscillation, J. Appl. Physiol. **56**, 553 (1984).

[4] J. Choi, G. Xia, M. H. Tawhai, E. A. Hoffman, and C.-L. Lin, Numerical study of high-frequency oscillatory air flow and convective mixing in a CT-based human airway model, Ann. Biomed. Eng. **38**, 3550 (2010).

[5] C. J. Roth, K. M. Förster, A. Hilgendorff, B. Ertl-Wagner, W. A. Wall, and A. W. Flemmer, Gas exchange mechanisms in preterm infants on HFOV—a computational approach, Sci. Rep. **8**, 13008 (2018).

[6] S. Jalal, T. Van de Moortele, O. Amili, and F. Coletti, Steady and oscillatory flow in the human bronchial tree, Phys. Rev. Fluids **5**, 063101 (2020).

[7] H. Luo and Y. Liu, Modeling the bifurcating flow in a CT-scanned human lung airway, J. Biomech. **41**, 2681 (2008).

[8] A. Banko, F. Coletti, D. Schiavazzi, C. Elkins, and J. Eaton, Three-dimensional inspiratory flow in the upper and central human airways, Exp. Fluids **56**, 117 (2015).

[9] A. Banko, F. Coletti, C. Elkins, and J. Eaton, Oscillatory flow in the human airways from the mouth through several bronchial generations, Int. J. Heat Fluid Flow **61**, 45 (2016).

[10] E. Nof, M. Heller-Algazi, F. Coletti, D. Waisman, and J. Sznitman, Ventilation-induced jet suggests biotrauma in reconstructed airways of the intubated neonate, J. R. Soc., Interface **17**, 20190516 (2020).

[11] E. R. Weibel, Geometric and dimensional airway models of conductive, transitory and respiratory zones of the human lung, in *Morphometry of the Human Lung* (Springer, Berlin, Heidelberg, 1963), pp. 136–142.

[12] N. Nowak, P. P. Kakade, and A. V. Annapragada, Computational fluid dynamics simulation of airflow and aerosol deposition in human lungs, Ann. Biomed. Eng. **31**, 374 (2003).

[13] D. K. Walters and W. H. Luke, A method for three-dimensional Navier-Stokes simulations of large-scale regions of the human lung airway, J. Fluids Eng. **132**, 051101 (2010).

[14] C. Kleinstreuer and Z. Zhang, An adjustable triple-bifurcation unit model for air-particle flow simulations in human tracheobronchial airways, J. Biomech. Eng. **131**, 021007 (2009).

[15] S. Jalal, A. Nemes, T. Van de Moortele, S. Schmitter, and F. Coletti, Three-dimensional inspiratory flow in a double bifurcation airway model, Exp. Fluids **57**, 148 (2016).

[16] S. Jalal, T. Van de Moortele, A. Nemes, O. Amili, and F. Coletti, Three-dimensional steady and oscillatory flow in a double bifurcation airway model, Phys. Rev. Fluids **3**, 103101 (2018).

[17] A. Menon, M. Weber, and H. Chang, Model study of flow dynamics in human central airways. Part III: Oscillatory velocity profiles, Respir. Physiol. **55**, 255 (1984).

[18] B. Gatlin, C. E. Cuicchi, J. R. Hammersley, D. E. Olson, R. N. Reddy, and G. G. Burnside, Computational simulation of steady and oscillating flow in branching tubes, ASME-Publications-FED **212**, 1 (1995).

[19] S. Berger, L. Talbot, and L.-S. Yao, Flow in curved pipes, Annu. Rev. Fluid Mech. **15**, 461 (1983).

[20] C. Jacob, D. G. Tingay, and J. S. Leontini, The impact of steady streaming and conditional turbulence on gas transport during high-frequency ventilation, Theor. Comput. Fluid Dyn. **35**, 265 (2021).

[21] D. Xu, B. Song, and M. Avila, Non-modal transient growth of disturbances in pulsatile and oscillatory pipe flows, J. Fluid Mech. **907**, R5 (2021).

[22] M. Hino, M. Sawamoto, and S. Takasu, Experiments on transition to turbulence in an oscillatory pipe flow, J. Fluid Mech. **75**, 193 (1976).

[23] R. Akhavan, R. Kamm, and A. Shapiro, An investigation of transition to turbulence in bounded oscillatory stokes flows part 1. experiments, J. Fluid Mech. **225**, 395 (1991).

[24] G. Vittori and R. Verzicco, Direct simulation of transition in an oscillatory boundary layer, J. Fluid Mech. **371**, 207 (1998).

[25] J. Canton, P. Schlatter, and Örlü, Modal instability of the flow in a toroidal pipe, J. Fluid Mech. **792**, 894 (2016).

[26] A. Gelfgat, Instability of steady flows in helical pipes, Phys. Rev. Fluids **5**, 103904 (2020).

[27] V. Lupi, J. Canton, and P. Schlatter, Global stability analysis of a 90°-bend pipe flow, Int. J. Heat Fluid Flow **86**, 108742 (2020).

[28] T. Pedley, Pulmonary fluid dynamics, Annu. Rev. Fluid Mech. **9**, 229 (1977).

[29] D. Jan, A. Shapiro, and R. Kamm, Some features of oscillatory flow in a model bifurcation, J. Appl. Physiol. **67**, 147 (1989).

[30] K. B. Heraty, J. G. Laffey, and N. J. Quinlan, Fluid dynamics of gas exchange in high-frequency oscillatory ventilation: in vitro investigations in idealized and anatomically realistic airway bifurcation models, Ann. Biomed. Eng. **36**, 1856 (2008).

[31] J. Grotberg, Pulmonary flow and transport phenomena, Annu. Rev. Fluid Mech. **26**, 529 (1994).

[32] B. B. Mandelbrot, *The Fractal Geometry of Nature* (WH Freeman New York, 1983), Vol. 173.

[33] J. Emery, The anatomy of the developing lung, Postgraduate Medical Journal **46**, 64 (1970).

[34] K. Koombua, R. M. Pidaparti, P. W. Longest, and K. R. Ward, Computational analysis of fluid characteristics in rigid and flexible human respiratory airway models, Eng. Appl. Comput. Fluid Mech. **2**, 185 (2008).

[35] J. R. Womersley, Method for the calculation of velocity, rate of flow and viscous drag in arteries when the pressure gradient is known, J. Physiol. **127**, 553 (1955).

[36] P. F. Fischer, F. Loth, S. E. Lee, S.-W. Lee, D. S. Smith, and H. S. Bassiouny, Simulation of high-Reynolds number vascular flows, Comput. Methods Appl. Mech. Eng. **196**, 3049 (2007).

[37] P. F. Fischer, J. W. Lottes, and S. G. Kerkemeier, Nek5000 web page (2008), https://nek5000.mcs.anl.gov/.

[38] S. E. Lee, S.-W. Lee, P. F. Fischer, H. S. Bassiouny, and F. Loth, Direct numerical simulation of transitional flow in a stenosed carotid bifurcation, J. Biomech. **41**, 2551 (2008).

[39] G. K. El Khoury, P. Schlatter, A. Noorani, P. F. Fischer, G. Brethouwer, and A. V. Johansson, Direct numerical simulation of turbulent pipe flow at moderately high Reynolds numbers, Flow, Turbul. Combust. **91**, 475 (2013).

[40] H. M. Tufo and P. F. Fischer, Terascale spectral element algorithms and implementations, in *ACM/IEEE SC 1999 Conference (SC'99)* (ACM, 1999), p. 68.

[41] P. C. Rimensberger, S. Schulzke, D. Tingay, and B. Von Ungern-Sternberg, *Pediatric and Neonatal Mechanical Ventilation* (Springer, Berlin Heidelberg, 2015), pp. 421–440.

[42] J. R. Hill and D. Robinson, Oxygen consumption in normally grown, small-for-dates and large-for-dates new-born infants, J. Physiol. **199**, 685 (1968).

[43] See Supplemental Material at http://link.aps.org/supplemental/10.1103/PhysRevFluids.8.123102 for animations corresponding to the evolution of isosurfaces of λ_2 vortical structures and the evolution of velocity magnitude $|\mathbf{U}|$

[44] J. Jeong and F. Hussain, On the identification of a vortex, J. Fluid Mech. **285**, 69 (1995).

[45] G. E. Karniadakis, G. Karniadakis, and S. Sherwin, *Spectral/hp Element Methods for Computational Fluid Dynamics* (Oxford University Press on Demand, 2005).

[46] A. N. Kolmogorov, The local structure of turbulence in incompressible viscous fluid for very large Reynolds numbers, Proc. Royal Society London. A Mathe. Physical Sci. **434**, 9 (1991).